PHYSICS AT THE TEVATRON*

Rick Field

Department of Physics, University of Florida
Gainesville, Florida, 32611, USA

(Received September 3, 2008)

The theme of the XXXIV International Meeting on Fundamental Physics on April 27, 2006 was "From HERA and the TEVATRON to the LHC". At that meeting I presented four lectures on "Physics at the Tevatron". This is a summary of two lectures on "Physics at the Tevatron: IMFP06 IMFP08" presented at the XXXVI International Meeting on Fundamental Physics held in Baeza, Spain on February 4–8, 2008. These two lectures are an attempt to highlight what we have learned at the Tevatron since my lectures in 2006. I will also look back at the "old days" of Feynman–Field collider phenomenology.

PACS numbers: 12.38.–t, 13.85.–t, 14.65.Ha, 14.70.–e

1. Introduction

The Tevatron, located at Fermilab near Chicago, Illinois, USA, collides protons with antiprotons at a center-of-mass energy of 1.96 TeV. As shown in Fig. 1, CDF and DØ are the two collider detector experiments at Fermilab. The Tevatron is currently the highest energy collider in the world and it has performed remarkably well over the past two years. At IMFP06 [1] the delivered integrated luminosity per month was about $92\,\mathrm{pb}^{-1}$ and at this meeting (IMFP08) it is about $165\,\mathrm{pb}^{-1}$, which corresponds to about 23 top-antitop pairs per month (see Table I and Fig. 2). At IMFP06 CDF and DØ had collected about $1.2\,\mathrm{fb}^{-1}$ of data. Two years later at IMFP08 the total integrated luminosity collected is about 2.8 fb^{-1}. This corresponds to an increase of about $1.6\,\mathrm{fb}^{-1}$ since IMFP06. More data has been collected since IMFP06 than had previously been collected in all of Run 2! At the Tevatron we are now measuring cross-sections that are at the 1 pb level or smaller, which is very exciting.

* Presented at the XXXVI International Meeting on Fundamental Physics, Baeza (Jaén), Spain, February 4–8, 2008.

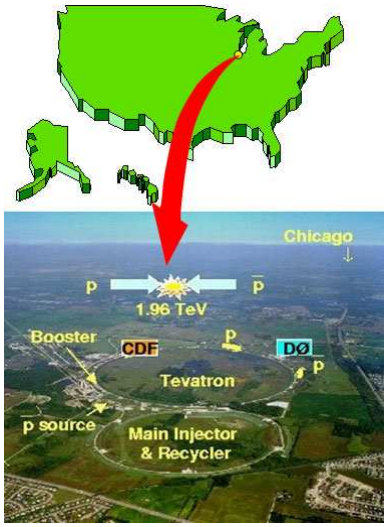

Fig. 1. Aerial photograph of the Tevatron, located at Fermilab near Chicago, Illinois, USA which collides protons with antiprotons at a center-of-mass energy of 1.96 TeV. CDF and DØ are the two collider detector experiments at Fermilab.

TABLE I

Tevatron luminosity at IMFP06 and IMFP08.

Luminosity records	IMFP06	IMFP08
Initial inst. lum	$1.8 \times 10^{32}\text{cm}^{-2}\text{s}^{-1}$	$2.9 \times 10^{32}\text{cm}^{-2}\text{s}^{-1}$
Integrated lum/week	25 pb^{-1}	45 pb^{-1}
Integrated lum/month	92 pb^{-1}	165 pb^{-1}

Many important new physics results have come from the Tevatron since IMFP06. For example, some of the CDF since IMFP06 are as follows:

- Observation of B_s-mixing: $\Delta m_s = 17.77 \pm 0.10$ (stat) ± 0.07 (sys).
- Observation of new baryon states: Σ_b and Ξ_b.
- Observation of new charmless: $B \to hh$ states.
- Evidence for D^0–$\bar{D}^0$ mixing.
- Precision W mass measurement: $M_W = 80.413\,\text{GeV}$ ($\pm 48\,\text{MeV}$).
- Precision Top mass measurement: $M_{\text{top}} = 170.5$ (± 2.2) GeV.
- W-width measurement: 2.032 (± 0.071) GeV.
- $W + Z$ discovery (6-sigma): $\sigma = 5.0$ (± 1.7) pb.
- $Z + Z$ evidence (3-sigma): $\sigma = 0.75 + 0.71 - 0.54$ pb.
- Single Top evidence (3-sigma) with 1.5 fb^{-1}: $\sigma = 3.0$ (± 1.2) pb.

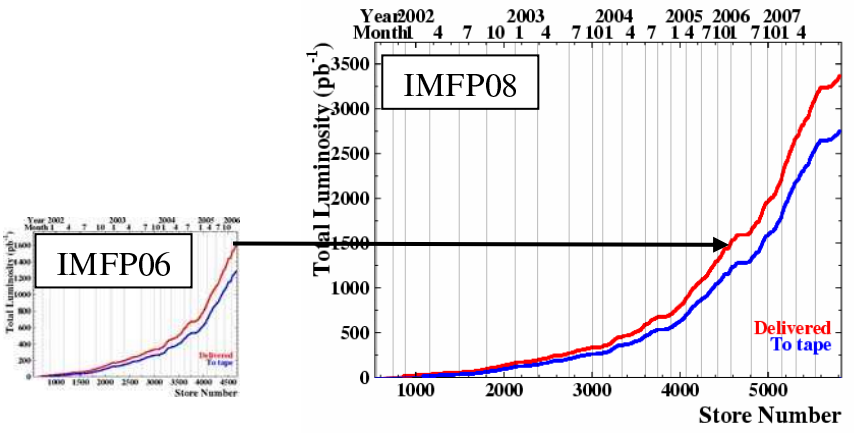

Fig. 2. Shows the total integrated luminosity delivered (and collected to tape by CDF) at the Tevatron at IMFP06 (left) and IMFP08 (right).

- $|V_{tb}| = 1.02 \pm 0.18$ (exp) ± 0.07 (th).
- Significant exclusions/reach on many BSM models.
- Constant improvement in Higgs Sensitivity.

I cannot possibly show all the interesting Tevatron results since IMFP06 in just two lectures. I will show a few of the many important Tevatron measurements and I will attempt to compare the recent results with what I showed at IMFP06. It is very interesting to see the improvement in just two years.

I will begin in Sec. 2 by taking a look back at the "old days" of Feynman–Field collider phenomenology. I think it is important for students to see how far we have come in our understanding of hadron–hadron collisions since 1973. In Sec. 3 I will show what we have learned about the "underlying event" in Run 2 at CDF. Sec. 4 will be devoted to vector boson production at the Tevatron and in Sec. 5 I will discuss top physics at the Tevatron.

2. From Feynman–Field to the Tevatron

When I arrived at CALTECH in 1973 it was already clear from SLAC deep inelastic scattering experiments that the proton was a composite particle made up of tiny hard pieces which were referred to as "partons". Also, there was mounting evidence that at least some of the partons were quarks. We knew that only about 50 % of the protons momentum was carried by the quarks, but I do not think we knew that the other 50 % was carried by point-like massless gluons. The ISR at CERN was studying proton–proton collisions at a center-of-mass energy of 53 GeV and Fermilab was colliding 200 GeV protons on fixed targets (*i.e.* $W = \sqrt{s} = 19.2\,\text{GeV}$).

When two protons of equal and opposite momentum collide at high energy most of the time they simply fall apart producing a collection of hadrons moving along the direction of the two incoming protons and all of the outgoing particles have small transverse momenta relative to the beam direction ($\sim 300\,\mathrm{GeV}/c$). However, it was noticed that occasionally a high transverse momentum, p_{T}, hadron (pion or kaon) would be produced. This did not happen often but it happened more often then one would expect if the proton was a "soft" object. In those days high transverse momentum meant anything with $p_{\mathrm{T}} > 2\,\mathrm{GeV}/c$ and the highest transverse momentums observed were only around $7\,\mathrm{GeV}/c$!

In about 1974 Feynman and I were wondering about where these high transverse momentum hadrons came from. We did not believe that a pion traveling in the direction of one of the incoming protons could "turn the corner" and come out at high transverse momentum without falling apart into its constituent quarks. We believed that the high p_{T} particles came from a hard 2-to-2 scattering of the quarks within the incoming protons. The two outgoing high transverse momentum quarks would then fragment into pions and kaons some of which would have high p_{T}. At that time we did not know how to calculate the quark–quark elastic scattering differential cross-section. The theory of Quantum Chromodynamics (QCD) was just beginning to be understood and the perturbative 2-to-2 parton–parton differential cross-sections had not yet been calculated. People were just beginning to realize that QCD was an asymptotically free theory which allows perturbation theory to be applied at high p_{T}. Because we did not yet understand how to calculate anything, in the first Feynman–Field paper (FF1) [2] which we completed in 1975, but did not publish until 1977 we concocted the "quark–quark elastic scattering black-box" model which is illustrated in Fig. 3. We fit the SLAC deep inelastic scattering data to determine the probability of finding a quark of flavor f within a proton carrying a fraction, x, of the protons momentum, $G_{p\to f}(x)$. In addition, we fit e^+e^- data to determine the probability that a hadron, h, carrying fractional momentum, z, of an outgoing quark of flavor, f, is contained among the fragmentation products, $F_{f\to h}(z)$. The proton structure functions (we called them quark distribution functions) and quark fragmentation functions (we called them quark decay functions) were assumed to scale (*i.e.* were a function only of the fractional momentum x or z). We took the quark–quark elastic scattering differential cross-section to be a "black-box" and determined it by fitting the data.

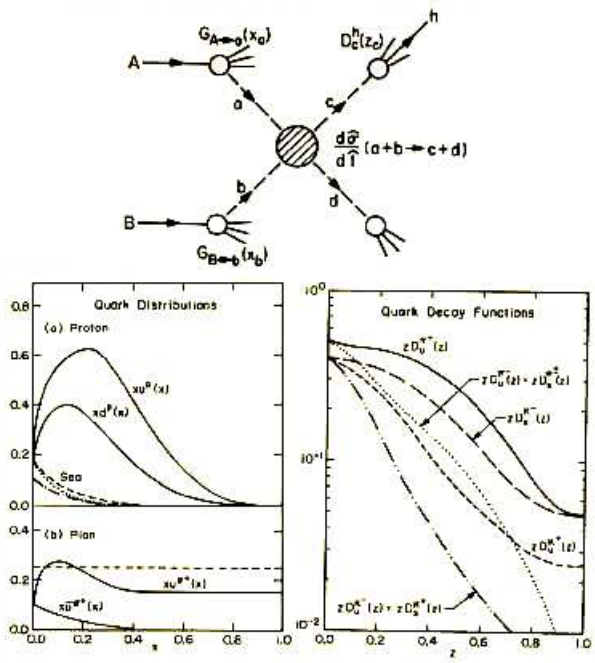

Fig. 3. Illustration of the Feynman–Field quark–quark elastic scattering "black-box" model for hadron–hadron collisions from FF1 (1977). (Top) The model assumed that high p_{T} particles arise from direct hard collisions between constituent quarks in the incoming particles, which fragment or cascade down into several hadrons. (bottom left) The quark distribution functions were determined by fitting the SLAC deep inelastic scattering data. (bottom right) The quark fragmentation functions were determined by fitting e^+e^- data and the 2-to-2 quark–quark elastic scattering cross-section, $d\sigma/dt$, was determined by fitting the data (*i.e.* "black-box").

I wrote the first draft of the Feynman–Field papers and Feynman would come in and give me sentences or paragraphs that he would like to include in the paper. The following is a Feynman quote from FF1: "*The model we shall choose is not a popular one, so that we will not duplicate too much of the work of others who are similarly analyzing various models (e.g. constituent interchange model, multiperipheral models, etc.). We shall assume that the high* p_{T} *particles arise from direct hard collisions between constituent quarks in the incoming particles, which fragment or cascade down into several hadrons.*"

The "black-box" model was naïve, however, it convinced us we were on the right track. As illustrated in Fig. 4, we adjusted the quark–quark elastic differential cross-section to fit the experimentally measured high p_{T} meson cross-section at $W = 19.4\,\mathrm{GeV}$ and then predicted it correctly at $W = 53\,\mathrm{GeV}$. The rise in the cross-section, of course, comes from the parton distribution function. We were amazed that we were able to use electron-proton and e^+e^- data to predict something about hadron–hadron collisions.

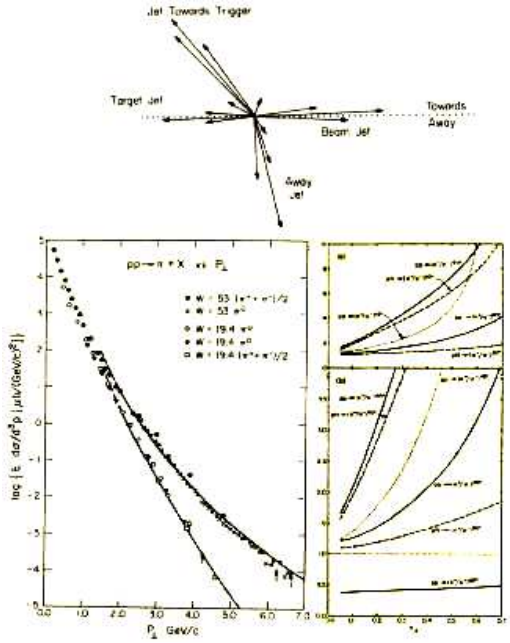

Fig. 4. (Top) Shows the topology predicted by the Feynman–Field quark–quark elastic scattering "black-box" model for hadron–hadron from FF1 (1977) in which there is a "toward" side "jet" (*i.e.* collection of hadrons moving roughly in the same direction) and an "away" jet, together with the beam and target jet (*i.e.* the "beam–beam" remnants). Also shows the predictions of the model for the inclusive meson cross-section at 19.4 GeV and 53 GeV (bottom left) and for the high $p_{\rm T}$ particle rations at 53 GeV (a) and 19.4 GeV (b).

The model also predicted the topology in high $p_{\rm T}$ hadron–hadron collisions that we are all familiar with today in which there is a "toward" side "jet" (*i.e.* collection of hadrons moving roughly in the same direction) and an "away" jet, together with the "beam–beam remnants" (we called them the beam and target jet). We studied this topology in more detail in FFF1 [3]. The "beam–beam remnants" are part of the "underlying event" in hadron–hadron collisions which I will discuss in Sec. 5.

In FF1 we were able to predict particle ratios at high $p_{\rm T}$. Actually, the reason we waited two years to publish the paper is that the model predicted the π^+/π^- ratio would increase at large $p_{\rm T}$ in proton–proton collisions and Feynman wanted to see some evidence of this before we published the paper. In July 1976 Feynman was at a meeting in Les Houches where he learned from Jim Cronin that the University of Chicago group did see the increase we expected in an experiment at Fermilab. The $x_{\rm T} = 2p_{\rm T}/W$ values at the ISR were too small to see much of an effect. I received a telegram which Feynman sent from Les Houches which stated: "*Saw Cronin — Am now convinced we're right track — Quick write — Feynman*".

We knew we were on the right track, but as you can see in retrospect there were many things we did not understand. For one, we thought the pion structure function went to a constant at high x and similarly we thought the quark fragmentation function to a pion went to a constant at large z. Of course, we all know now that there can be a constant term in these functions, but they are the so-called "higher twist" terms and fall off as a power of Q^2. Also, the "black-box" model did not include gluons. At that time we did not realize the gluon is a "hard" point-like parton just like the quark. We thought of it more like "glue".

The "black-box" model lasted less than a year. Things were happening fast. Even before the paper was published we were learning more about QCD. Once we realized it is an asymptotically free theory and that we could use perturbation theory to calculate high p_{T} phenomena we did everything over again, but this time using QCD as illustrated in Fig. 5. The parton distribution functions (PDF's) and the fragmentation functions now depended on the scale of the hard scattering (*i.e.* Q^2). Gluons were now included and all of the seven parton–parton scattering differential cross-sections were

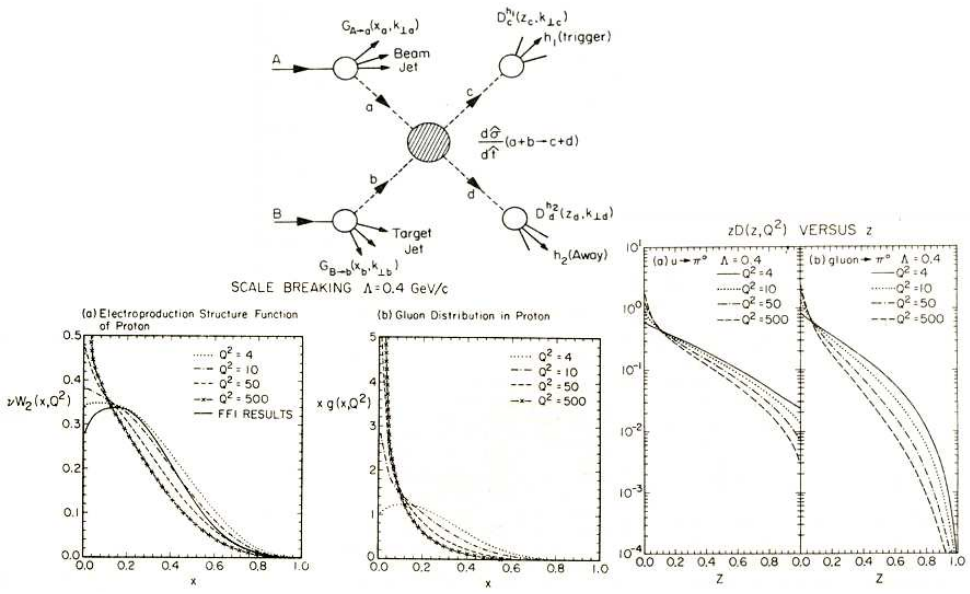

Fig. 5. Illustration of the QCD model for hadron–hadron collisions from FFF2 (1978). (Top) the model assumed that high p_{T} particles arise from direct hard collisions between constituent quarks and gluons in the incoming particles, which fragment into "jets" of hadrons. (Bottom left) the quark distribution functions were determined by fitting the SLAC deep inelastic scattering data at $Q^2 = 4\,\mathrm{GeV}$ and determined at other values of Q^2 using QCD perturbation theory. (Bottom right) the quark fragmentation functions were determined by fitting e^+e^- data and the 2-to-2 quark–quark elastic scattering cross-section, ds/dt, was determined from the data (*i.e.* "black-box").

calculated by perturbation theory. Fig. 6 shows some of the predictions of the QCD approach with $\Lambda = 400\,\text{MeV}$ from FFF2 (1978) [4, 5]. We realized that the "jet" cross-section was much larger than the cross-section to produce a single charged hadron at the same p_{T}. We did not know if they would ever build a collider with a center-of-mass energy of 1 TeV, but as can be seen in Fig. 6, in 1978 we predicted the "jet" cross-section at $W = 1\,\text{TeV}$. However, our transverse momentum scale only extended out to $30\,\text{GeV}/c$! The prediction at $p_{\text{T}} = 30\,\text{GeV}/c$ is shown on the recent inclusive jet cross-section measured at CDF. Due to the resolution of the CDF calorimeter it is difficult to measure the jet cross-section below $60\,\text{GeV}/c$. What we thought in 1978 was a high p_{T} jet is too low of a p_{T} to be measured at the Tevatron! Fig. 7 shows a "lego" plot of a high p_{T} di-jet event measured in the CDF calorimeter. Comparing Fig. 4 with the CDF jet data shows the wonderful journey from $7\,\text{GeV}/c$ π^0's to $600\,\text{GeV}/c$ jets! The CDF the high p_{T} jet events are a bit "cleaner" than we would have thought back in 1978. This is because at that time we were using a QCD scale of around 400 MeV and today we know that it is much smaller (around $\sim 200\,\text{MeV}$). Small Λ means a small QCD coupling α_{s} and hence less initial and final state gluon radiation, resulting in "cleaner" di-jet events. The following is a Feynman quote from FFF2: "*At the time of this writing, there is still no sharp quantitative test of QCD. An important test will come in connection with the phenomena of high* p_{T} *discussed here.*"

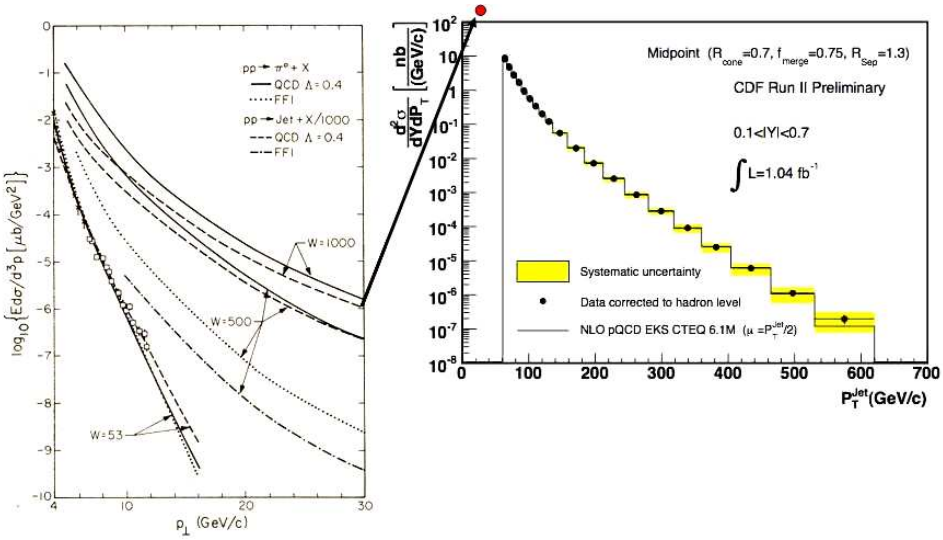

Fig. 6. (Left) Predictions of the QCD model for meson and "jet" production hadron–hadron collisions from FFF2 (1978). (Right) CDF Run 2 data on the inclusive "jet" cross-section at 1.96 TeV with an integrated luminosity of $1\,\text{fb}^{-1}$.

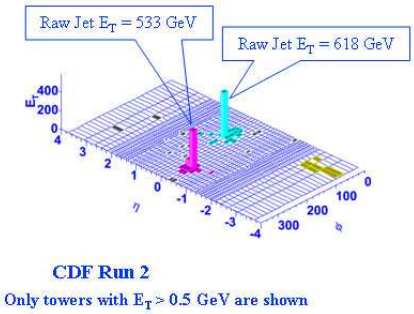

Fig. 7. CDF Run 2 di-jet event at 1.96 TeV with (raw) jet transverse energies of 403 GeV and 322 GeV observed in July 2002.

Fig. 8 illustrates the way the modern QCD Monte Carlo models simulate a proton–antiproton collision in which a "hard" 2-to-2 parton scattering with transverse momentum, p_{T} (hard), has occurred. The "hard scattering" com-

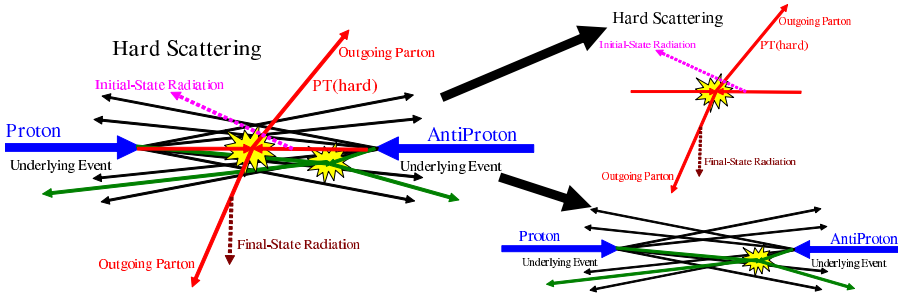

Fig. 8. Illustration of the way QCD Monte Carlo models simulate a proton–antiproton collision in which a "hard" 2-to-2 parton scattering with transverse momentum, p_{T} (hard), has occurred. The "hard scattering" component of the event consists of particles that result from the hadronization of the two outgoing partons (*i.e.* the initial two "jets") plus the particles that arise from initial and final state radiation it (*i.e.* multijets). The "underlying event" consists of particles that arise from the "beam–beam remnants" and from multiple parton interactions.

ponent of the event consists of particles that result from the hadronization of the two outgoing partons (*i.e.* the initial two "jets") plus the particles that arise from initial and final state radiation (*i.e.* multijets). The "underlying event" consists of particles that arise from the "beam–beam remnants" and from multiple parton interactions (MPI). Of course, in a given event it is not possible to uniquely determine the origin of the outgoing particles and whatever observable one chooses to study inevitably receives contributions from both the hard component and the underlying event. I will discuss the tuning of the QCD Monte Carlo model generators to fit the CDF "underlying event" data in Sec. 5.

Experimentally we measure "jets" at the detector level (*i.e.* calorimeter level) by observing the energy in each calorimeter cell as illustrated in Fig. 9. Of course, the "jet" cross-section depends on ones choice of jet algorithm.

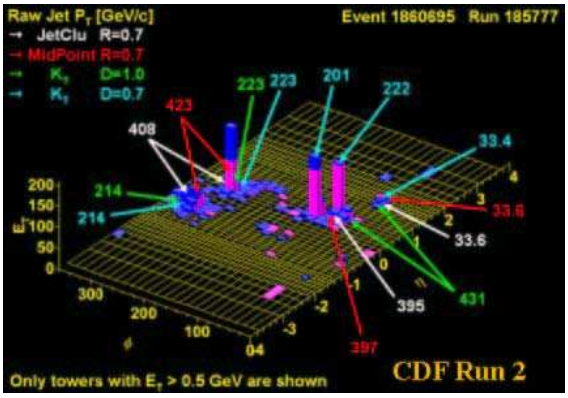

Fig. 9. Shows the transverse energy of calorimeter towers with $E_{\rm T} > 0.5\,{\rm GeV}$ for an event in the CDF detector. The MidPoint algorithm combines the two clusters into one "jet" with $p_{\rm T} = 423\,{\rm GeV}/c$ while the $K_{\rm T}$ algorithm ($D = 0.7$) finds two "jets" with $p_{\rm T} = 223\,{\rm GeV}/c$ and $214\,{\rm GeV}/c$.

Each jet algorithm is a different observable and comparing the results of different jet algorithm teaches us about QCD. Of course, what is measured in the calorimeter must be corrected for detector efficiency which is done by comparing the QCD Monte Carlo models at the particle (*i.e.* generator level) with the result after detector simulation. I believe that experimenters should publish what they measure (*i.e.* observables at the particle level with the "underlying event"). However, to determine the parton distribution functions accurately one must calculate at next-to-leading order (NLO). At present there is no QCD Monte Carlo generator at NLO (*i.e.* MC@NLO) for the production of light quarks and gluons in hadron–hadron collisions. At present, the NLO parton level does not have fragmentation or an "underlying event". There are three approaches for comparing data corrected to the particle level (*i.e.* hadron level) with parton level calculations.

The first approach is to neglect the difference and to compare the hadron level data directly with the parton level calculation. Fig. 10 shows the inclusive jet cross-section using the MidPoint algorithm ($R = 0.7$, $f_{\rm merge} = 0.5$) for two rapidity bins as measured by DØ. At IMFP06 ($\mathcal{L} = 378\,{\rm pb}^{-1}$) DØ compared the experimentally measured hadron level prediction directly with the NLO parton level theory curves and assumed that the parton level to hadron level corrections were small for jets above 50 GeV. At IMFP08 ($\mathcal{L} = 0.9\,{\rm fb}^{-1}$) DØ corrected for hadronization and threshold effects. Fig. 11 shows the data divided by the corrected data for the two rapidity ranges.

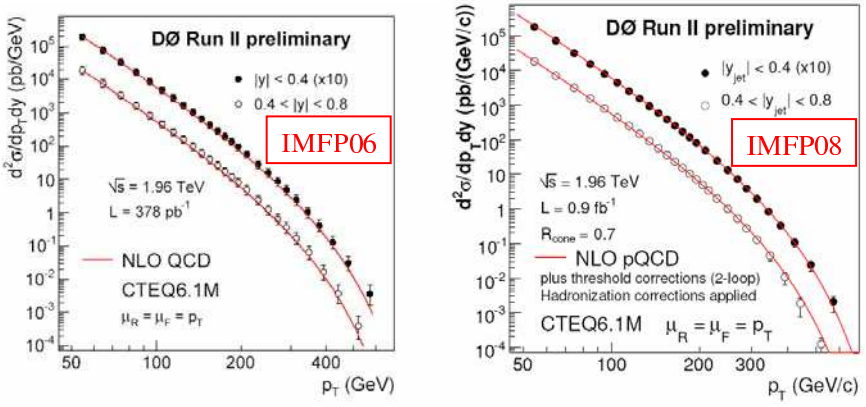

Fig. 10. The DØ Run 2 inclusive jet cross-section using the MidPoint algorithm ($R = 0.7, f_{\mathrm{merge}} = 0.50$) compared with parton-level NLO QCD. At IMFP06 the integrated luminosity was $378\,\mathrm{pb}^{-1}$ (left) and at IMFP08 it is $0.9\,\mathrm{fb}^{-1}$ (right). At IMFP06 the hadron-level data were compared directly with the parton-level NLO QCD, whereas at IMFP08 the NLO parton level theory is corrected for hadronization and threshold effects.

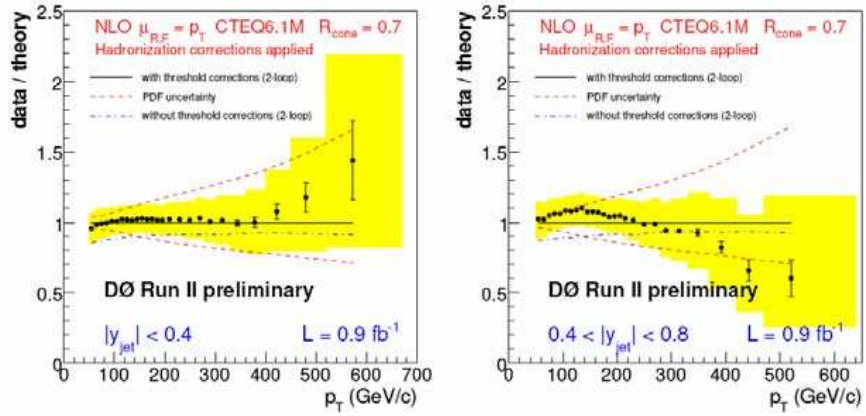

Fig. 11. Data divided by theory for the corrected DØ Run 2 inclusive jet cross-section using the MidPoint algorithm ($R = 0.7, f_{\mathrm{merge}} = 0.50$) compared with parton-level NLO QCD for $|Y_{\mathrm{jet}}| < 0.4$ (left) and $0.4 < |Y_{\mathrm{jet}}| < 0.8$ (right).

Another approach for comparing what is measured at the particle level in the detector with the NLO parton level theory is to use the QCD Monte Carlo models to determine the parton to hadron correction factor. This factor $C_{\mathrm{parton}\to\mathrm{hadron}}$ includes the effects from the "underlying event" and fragmentation. After determining this correction factor one can either extrapolate the data to the particle level (by multiplying by the reciprocal of this factor) or extrapolate the NLO QCD parton level theory to the hadron level (by multiplying by this factor). Fig. 12 shows the inclusive jet cross-

section using the MidPoint algorithm ($R = 0.7$, $f_{\text{merge}} = 0.75$) in the central region as measured by CDF at the hadron level compared with the NLO QCD prediction corrected to the hadron level. The measured integrated

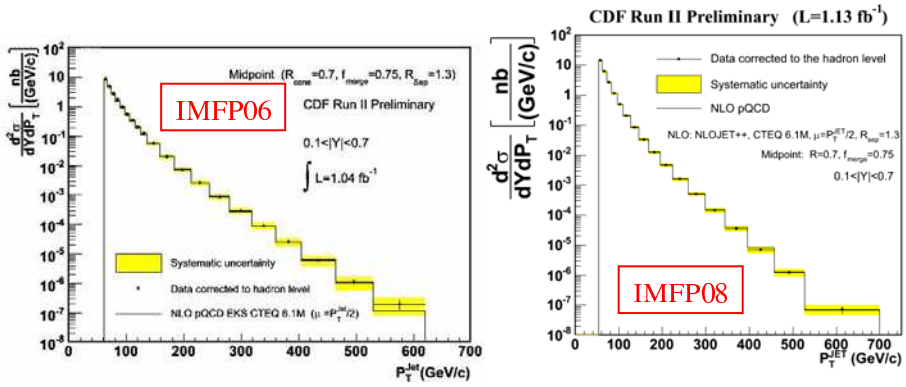

Fig. 12. The CDF Run 2 inclusive jet cross-section using the MidPoint algorithm ($R = 0.7$, $f_{\text{merge}} = 0.75$) compared with with NLO QCD. The data are at the hadron level and the NLO QCD parton level theory (CTEQ61M) has been corrected for fragmentation effects and for the "underlying event". At IMFP06 the integrated luminosity was 1.04 fb^{-1} (left) and at IMFP08 it is 1.13 fb^{-1} (right).

cross-section for $p_{\text{T}}(\text{jet}) > 525\,\text{GeV}/c$ is about $15\,\text{fb}^{-1}$! Fig. 13 shows the data divided by the theory and the parton to hadron correction factor. The corrections are significant for $p_{\text{T}}(\text{jet}) < 300\,\text{GeV}/c$ (they come mostly from the "underlying event").

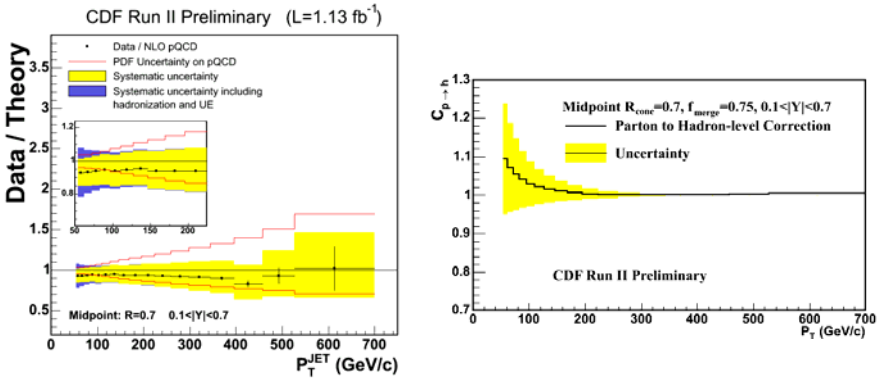

Fig. 13. Data divided by theory for the CDF Run 2 inclusive jet cross-section using the MidPoint algorithm ($R = 0.7$, $f_{\text{merge}} = 0.75$) (left). The data have been extrapolated (*i.e.* corrected) to the parton level using the parton to hadron correction factor (right). The hadron-level data are multiplied by the reciprocal of this factor.

Fig. 14 compares ratio of data divided by theory for the central inclusive jet cross-section as measured by CDF and DØ. Although both CDF and DØ

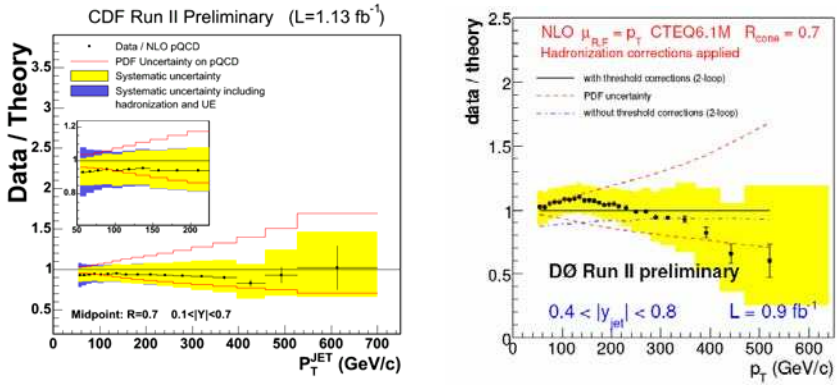

Fig. 14. Data divided by theory for the CDF Run 2 inclusive jet cross-section using the MidPoint algorithm ($R = 0.7, f_{\rm merge} = 0.75$) from Fig. 13 (left) and the DØ Run 2 inclusive jet cross-section using the MidPoint algorithm ($R = 0.7, f_{\rm merge} = 0.50$) from Fig. 11 (right).

show good agreement with theory it is clear from Fig. 14 that the CDF and DØ cross-sections are slightly different. For CDF data/theory is less than one, while for DØ it is greater than one (for $p_{\rm T}({\rm jet}) < 250\,{\rm GeV}/c$). This might be due to the fact that DØ has not removed the "underlying event".

Fig. 15 shows the CDF Run 2 di-jet invariant mass cross-section using the MidPoint algorithm ($R = 0.7, f_{\rm merge} = 0.75$) at the hadron level compared with the NLO QCD prediction corrected to the hadron level using the parton to hadron correction factor shown in the figure.

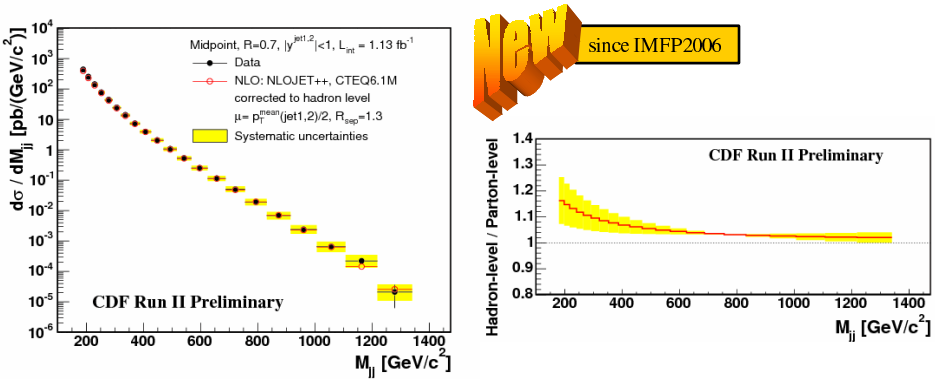

Fig. 15. The CDF Run 2 di-jet invariant mass cross-section using the MidPoint algorithm ($R = 0.7, f_{\rm merge} = 0.75$) compared with NLO QCD (left). The data are at the hadron level and the NLO QCD parton level theory (CTEQ61M) has been corrected for fragmentation effects and for the "underlying event" using the parton to hadron correction factor (right). The parton level NLO QCD theory is multiplied by the this factor. This analysis is new since IMFP06.

This analysis uses 1.13 fb^{-1} and is new since IMFP06. Fig. 16 compares ratio of data divided by theory for the central inclusive jet cross-section with the ratio of data divided by theory for the di-jet invariant mass cross-section, both measured by CDF. Both show good agreement with theory. However, it is interesting that for the inclusive jet cross-section data/theory is less than one, while for the di-jet invariant mass cross-section it is greater than one. This may be related to the fact that the QCD Monte Carlo models slightly underestimate the individual jet masses.

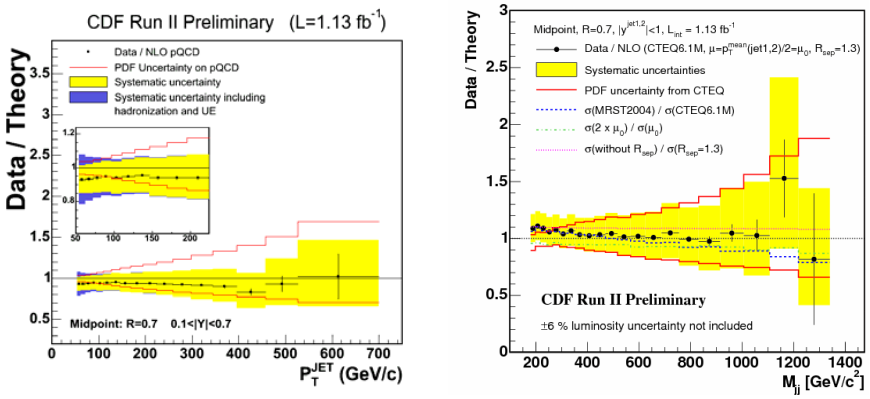

Fig. 16. Data divided by theory for the CDF Run 2 inclusive jet cross-section using the MidPoint algorithm ($R = 0.7, f_{\rm merge} = 0.75$) from Fig. 13 (left) and the CDF Run 2 di-jet invariant mass cross-section using the MidPoint algorithm ($R = 0.7, f_{\rm merge} = 0.75$) (right).

Fig. 17 shows the lego plot for an amazing CDF Rune 2 di-jet event in which the two jet transverse energies are 666 GeV and 633 GeV, respectively, with a di-jet invariant mass of 1.364 TeV. This event has $M_{jj}/E_{\rm CM} \approx 70\,\%$! In contrast to this, Fig. 18 shows one of the 16 CDF Run 2 exclusive $p + p \to p + p + e^+ + e^-$ candidate events corresponding to a cross-section of $\sigma = 1.6 \pm 0.3\,{\rm pb}$. Here there is no activity in the calorimeter except for the electron–positron pair. Both the di-jet and exclusive electron–positron pair analyses are new since IMFP06.

Fig. 19 shows the CDF Run 2 inclusive jet cross-section using the $K_{\rm T}$ algorithm at IMFP06 ($\mathcal{L} = 385$ pb^{-1}) and IMFP08 ($\mathcal{L} = 1.0$ fb^{-1}). The data are measured at five rapidity ranges, with the most forward being $1.6 < |Y_{\rm jet}| < 2.1$. The data are at the particle (*i.e.* hadron level) and the NLO parton level theory has been corrected to the particle level. As for the MidPoint algorithm, the parton level to hadron level corrections are significant for $p_{\rm T}$ (jet) $< 300\,{\rm GeV}/c$ (coming mostly from the "underlying event"). The agreement between the theory and data is good. Most theorists prefer the $K_{\rm T}$ algorithm over cone algorithms, however, it must be demonstrated that the $K_{\rm T}$ algorithm will work in the collider environment where there is

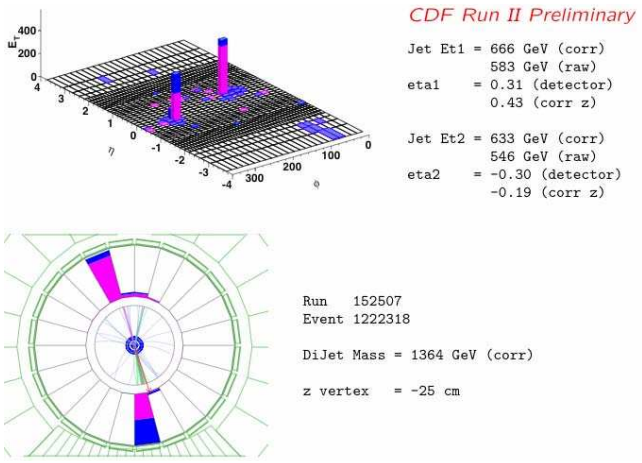

Fig. 17. A recent CDF Run 2 di-jet event at 1.96 TeV with (corrected) jet transverse energies of 666 GeV and 633 GeV and with a di-jet invariant mass of 1.364 TeV (this event has $M_{jj}/E_{\mathrm{CM}} \approx 70\%$!).

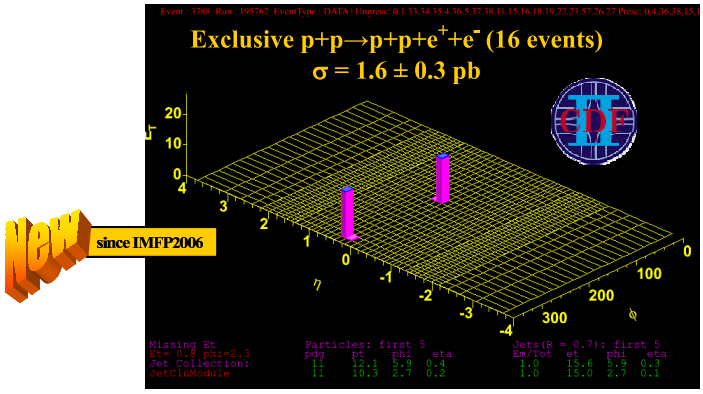

Fig. 18. One of the 16 CDF Run 2 exclusive $p + p \to p + p + e^+ + e^-$ candidate events corresponding to a cross-section of $\sigma = 1.6 \pm 0.3$ pb. This analysis is new since IMFP06.

an "underlying event". Fig. 19 shows that the K_{T} algorithm works fine at the Tevatron. The parton to hadron correction factors for the K_{T} algorithm are similar to the MidPoint algorithm correction factors.

Fig. 20 shows the CDF Run 2 forward inclusive jet cross-section using the MidPoint algorithm ($R = 0.7, f_{\mathrm{merge}} = 0.75$) compared NLO QCD. The NLO QCD theory has been extrapolated (*i.e.* corrected) to the hadron level. This data is new since IMFP06. Fig. 21 shows the data divided by theory for the CDF Run 2 forward inclusive jet cross-section using the K_{T} algorithm ($D = 0.7$) and the CDF Run 2 forward inclusive jet cross-section using the MidPoint algorithm ($R = 0.7, f_{\mathrm{merge}} = 0.75$). The very forward region puts constraints on the high x gluon distribution within protons and antiprotons.

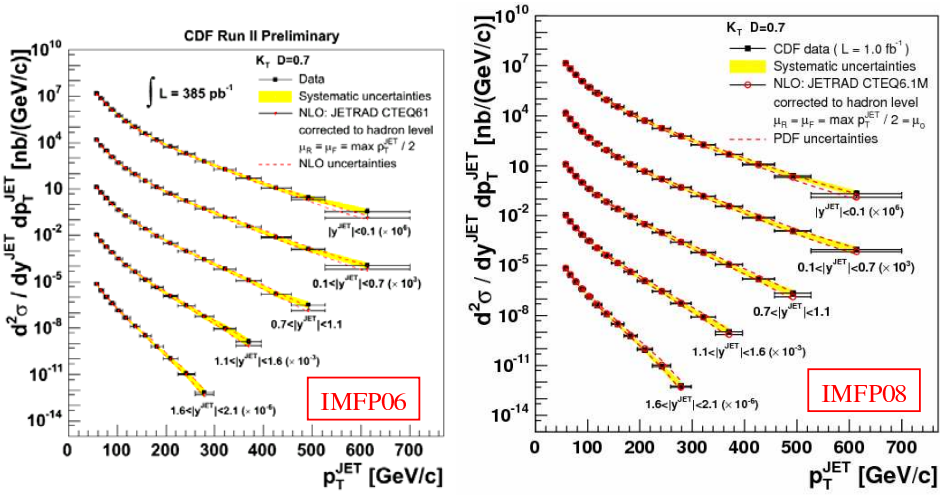

Fig. 19. The CDF Run 2 forward inclusive jet cross-section using the $K_{\rm T}$ algorithm with $D = 0.5$. The data are at the hadron level (with an "underlying event") and the NLO parton level theory (CTEQ61M) has been corrected for fragmentation effects and for the "underlying event". At IMFP06 the integrated luminosity was 385 pb^{-1} (left) and at IMFP08 it is 1.0 fb^{-1} (right).

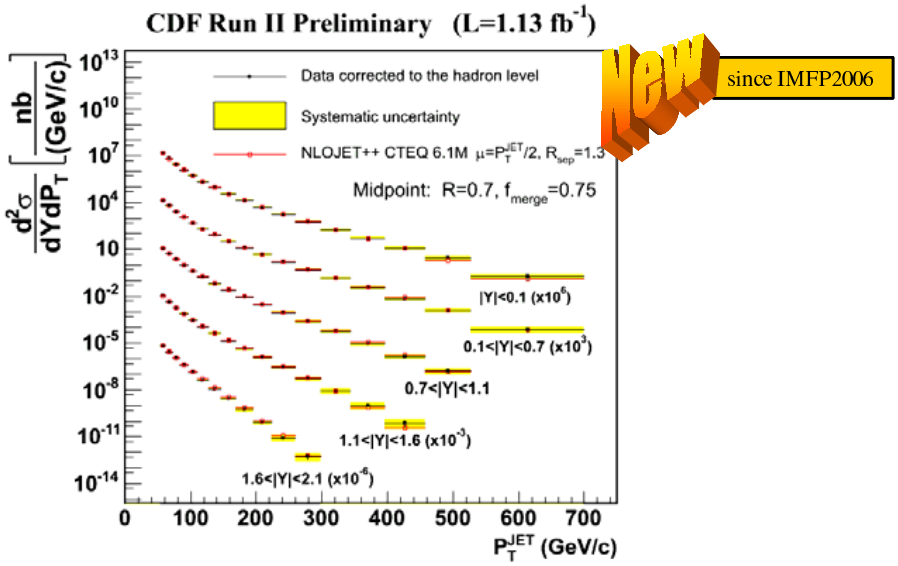

Fig. 20. The CDF Run 2 forward inclusive jet cross-section using the MidPoint algorithm ($R = 0.7, f_{\rm merge} = 0.75$) compared NLO QCD. The data are at the hadron level and the NLO QCD parton level theory (CTEQ61M) has been corrected for fragmentation effects and for the "underlying event". This analysis is new since IMFP06.

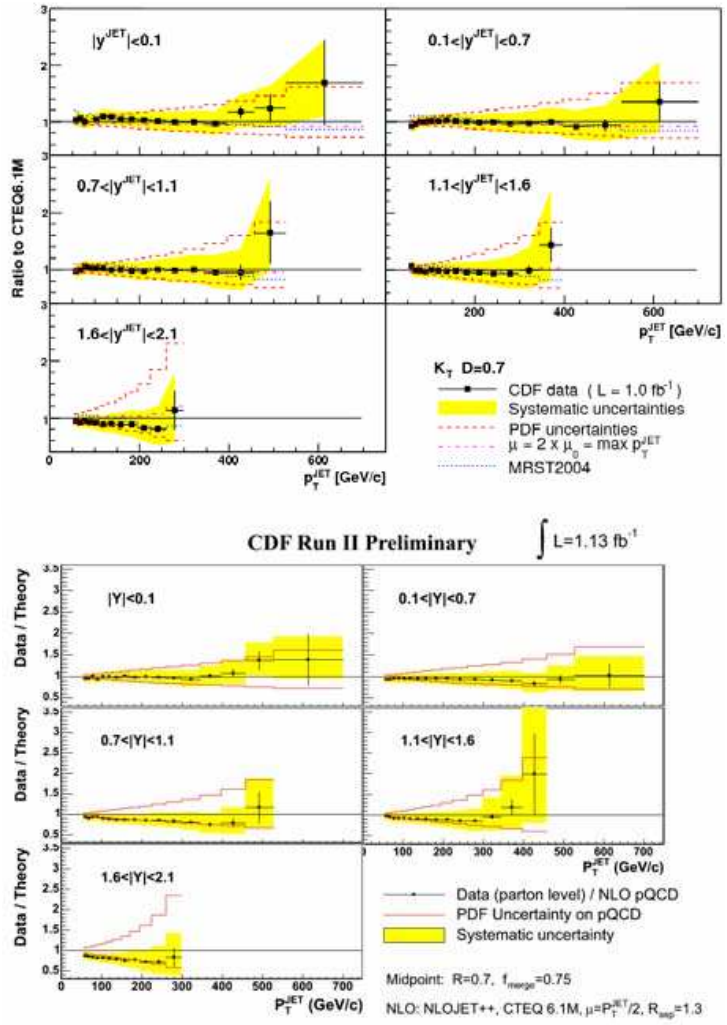

Fig. 21. Data divided by theory for the CDF Run 2 forward inclusive jet cross-section using the K_{T} algorithm ($D = 0.7$) (top) and the CDF Run 2 forward inclusive jet cross-section using the MidPoint algorithm ($R = 0.7$, $f_{\mathrm{merge}} = 0.75$) (bottom).

3. Studying the underlying event at CDF

In order to find "new" physics at a hadron–hadron collider it is essential to have Monte Carlo models that simulate accurately the "ordinary" QCD hard-scattering events [6–9]. To do this one must not only have a good model of the hard scattering part of the process, but also of the beam–beam remnants and the multiple parton interactions (MPI). The "underlying event" is an unavoidable background to most collider observables and a good

understanding of it will lead to more precise measurements at the Tevatron and the LHC. We have learned that at the Tevatron both the inclusive jet cross-section and the b-jet cross-section depend sensitively on the "underlying event". At CDF we are working to understand and model the "underlying event" at the Tevatron. We are also trying to extrapolate what we are learning at the Tevatron to the LHC. To study the "underlying event" in high transverse momentum jet production we use the topological structure of hard scattering event [10–12]. The direction of the leading calorimeter jet is used to isolate regions of η–ϕ space that are sensitive to the "underlying event". As illustrated in Fig. 22, the direction of the leading jet, jet#1, is used to define correlations in the azimuthal angle, $\Delta\phi$. The angle $\Delta\phi = \phi - \phi_{\text{jet\#1}}$ is the relative azimuthal angle between a charged particle and the direction of jet#1. The "transverse" region is almost perpendicular to the plane of the hard 2-to-2 scattering and is therefore very sensitive to the "underlying event". Furthermore, we consider two classes of events. We refer to events in which there are no restrictions placed on the second and third highest p_{T} jets (jet#2 and jet#3) as "leading jet" events. Events with at least two jets with $p_{\text{T}} > 15\,\text{GeV}$ where the leading two jets are nearly "back-to-back" ($|\Delta\phi_{12}| > 150^\circ$) with $p_{\text{T}}(\text{jet\#2})/p_{\text{T}}(\text{jet\#1}) > 0.8$ and $p_{\text{T}}(\text{jet\#3}) < 15\,\text{GeV}$ are referred to as "back-to-back" events. "Back-to-back" events are a subset of the "leading jet" events. The idea here is to suppress hard initial and final-state radiation thus increasing the sensitivity of the "transverse" region to the "beam–beam remnant" and the multiple parton scattering component of the "underlying event".

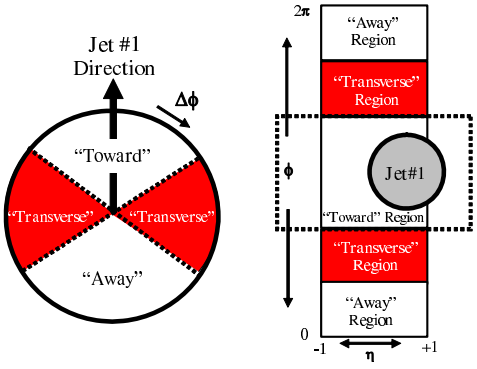

Fig. 22. Illustration of correlations in azimuthal angle relative to the direction of the leading jet (MidPoint, $R = 0.7$, $f_{\text{merge}} = 0.75$) in the event, jet#1. The angle $\Delta\phi = \phi - \phi_{\text{jet\#1}}$ is the relative azimuthal angle between charged particles (or calorimeter towers) and the direction of jet#1. The "transverse" region is defined by $60^\circ < |\Delta\phi| < 120^\circ$ and $|\eta| < 1$. We examine charged particles in the range $p_{\text{T}} > 0.5\,\text{GeV}/c$ and $|\eta| < 1$, but allow the leading jet to be in the region $|\eta(\text{jet\#1})| < 2$.

As illustrated in Fig. 23, we define a variety of MAX and MIN "transverse" regions which helps separate the "hard component" (initial and final-state radiation) from the "beam–beam remnant" component. MAX (MIN) refer to the "transverse" region containing the largest (smallest) number of charged particles or the region containing the largest (smallest) scalar p_{T} sum of particles. Since we will be studying regions in η–ϕ space with different areas, we construct densities by dividing by the area. For example, the charged particle density, $dN/d\eta d\phi$, corresponds number of charged particle with $p_{\mathrm{T}} > 0.5\,\mathrm{GeV}/c$ per unit η–ϕ, and the p_{T} sum density, $dp_{\mathrm{T\ sum}}/d\eta d\phi$, corresponds the amount of charged particle ($p_{\mathrm{T}} > 0.5\,\mathrm{GeV}/c$) scalar $p_{\mathrm{T\ sum}}$ per unit $\eta - \phi$. The overall "transverse" region defined in Fig. 22 includes both the "transMAX" and the "transMIN" region. One expects that "transMAX" will pick up the hardest initial or final-state radiation while both "transMAX" and "transMIN" should receive "beam–beam remnant" contributions. Hence one expects "transMIN" to be more sensitive to the "beam–beam remnant" component of the "underlying event", while the "transMAX" minus the "transMIN" (*i.e.* "transDIF") is very sensitive to initial and final-state radiation. This idea, was first suggested by Bryan Webber, and implemented in a paper by Pumplin [13]. Also, Valaria Tano studied this in her CDF Run 1 analysis of maximum and minimum transverse cones [14].

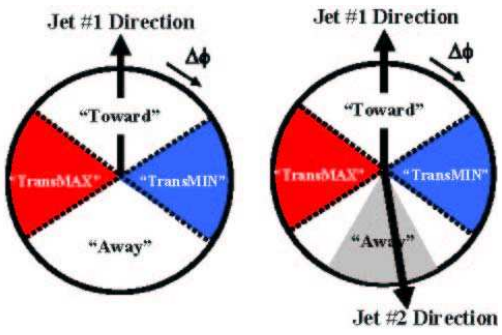

Fig. 23. Illustration of correlations in azimuthal angle $\Delta\phi$ relative to the direction of the leading jet (highest p_{T} jet) in the event, jet#1 for "leading jet" events (left) and "back-to-back" events (right). Events in which there are no restrictions placed on the on the second highest p_{T} jet, jet#2, are referred to as "leading jet" events. Events with at least two jets where the leading two jets are nearly "back-to-back" ($\Delta\phi_{12} > 150^{\circ}$) with $p_{\mathrm{T}}(\mathrm{jet}\#2)/p_{\mathrm{T}}(\mathrm{jet}\#1) > 0.8$ and $p_{\mathrm{T}}(\mathrm{jet}\#3) < 15\,\mathrm{GeV}/c$ are referred to as "back-to-back" events. In both cases the angle $\Delta\phi = \phi - \phi_{\mathrm{jet}\#1}$ is the relative azimuthal angle between charged particles and the direction of jet#1. On an event by event basis, we define "transMAX" ("transMIN") to be the maximum (minimum) of the two "transverse" regions, $60^{\circ} < \Delta\phi < 120^{\circ}$ and $60^{\circ} < -\Delta\phi < 120^{\circ}$. "TransMAX" and "transMIN" each have an area in $\eta - \phi$ space of $\Delta\eta\Delta\phi = 4\pi/6$. The overall "transverse" region defined in Fig. 22 includes both the "transMAX" and the "transMIN" region.

Fig. 24 and Fig. 25 show the CDF Run 2 data on the density of charged particles and the charged p_{T} sum density in the "transMAX" and "transMIN" regions for "leading jet" and "back-to-back" events. The data are compared with PYTHIA Tune A (with multiple parton interactions) and HERWIG (without multiple parton interactions). PYTHIA Tune A was determined by fitting the CDF Run 1 "underlying event" data [10].

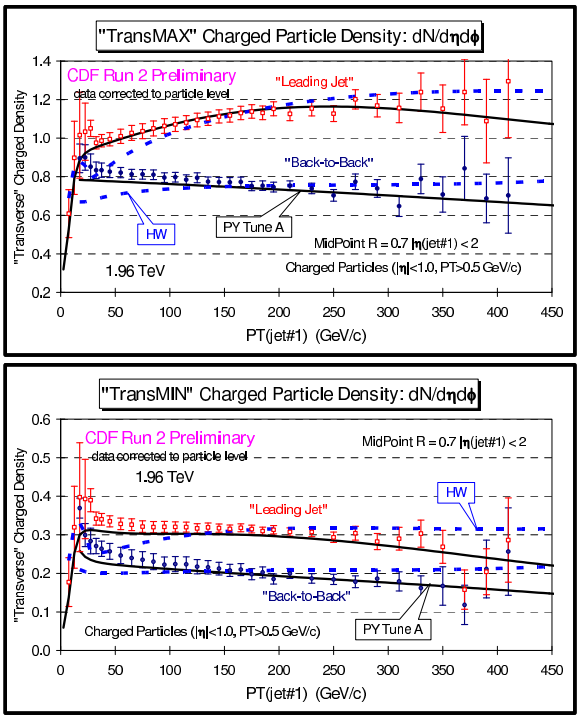

Fig. 24. CDF Run 2 data at 1.96 TeV on charged particle density, $dN/d\eta d\phi$, with $p_{\mathrm{T}} > 0.5\,\mathrm{GeV}/c$ and $|\eta| < 1$ in the "transMAX" region (top) and the "transMIN" region (bottom) for "leading jet" and "back-to-back" events as defined in Fig. 23 as a function of the leading jet p_{T} compared with PYTHIA Tune A and HERWIG. The data are corrected to the particle level (*with errors that include both the statistical error and the systematic uncertainty*) and compared with the theory at the particle level (*i.e.* generator level).

As expected, the "leading jet" and "back-to-back" events behave quite differently. For the "leading jet" case the "transMAX" densities rise with increasing $p_{\mathrm{T}}(\mathrm{jet}\#1)$, while for the "back-to-back" case they fall with increasing $p_{\mathrm{T}}(\mathrm{jet}\#1)$. The rise in the "leading jet" case is, of course, due to hard initial and final-state radiation, which has been suppressed in the "back-to-back" events. The "back-to-back" events allow for a more close look at the "beam–beam remnant" and multiple parton scattering component of the "underlying event" and PYTHIA Tune A does a better job describing the data than HERWIG.

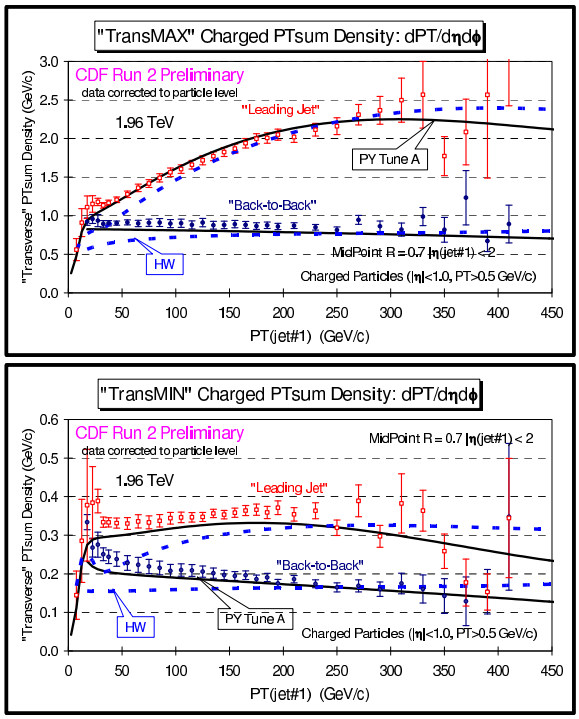

Fig. 25. CDF Run 2 data at 1.96 TeV on scalar p_{T} sum density of charged particles, $dp_{\mathrm{T}}/d\eta d\phi$, with $p_{\mathrm{T}} > 0.5\,\mathrm{GeV}/c$ and $|\eta| < 1$ in the "transMAX" region (top) and the "transMIN" region (bottom) for "leading jet" and "back-to-back" events as defined in Fig. 23 as a function of the leading jet p_{T} compared with PYTHIA Tune A and HERWIG. The data are corrected to the particle level (with errors that include both the statistical error and the systematic uncertainty) and compared with the theory at the particle level (*i.e.* generator level).

The "transMIN" densities are more sensitive to the "beam–beam remnant" and multiple parton interaction component of the "underlying event". The "back-to-back" data show a decrease in the "transMIN" densities with increasing $p_{\mathrm{T}}(\mathrm{jet}\#1)$ which is described fairly well by PYTHIA Tune A but not by HERWIG. The decrease of the "transMIN" densities with increasing $p_{\mathrm{T}}(\mathrm{jet}\#1)$ for the "back-to-back" events is very interesting and might be due to a "saturation" of the multiple parton interactions at small impact parameter. Such an effect is included in PYTHIA Tune A but not in HERWIG (without multiple parton interactions).

Fig. 26 and Fig. 27 compares the CDF Run 2 data on the density of charged particles and the charged p_{T} sum density for "transDIF" and for the overall "transverse" region, respectively, with PYTHIA Tune A and HERWIG for "leading jet" and "back-to-back" events. The average p_{T} for charged particles with with $p_{\mathrm{T}} > 0.5\,\mathrm{GeV}/c$ and $|\eta| < 1$ in the overall "transverse" region for "leading jet" and "back-to-back" events are compared

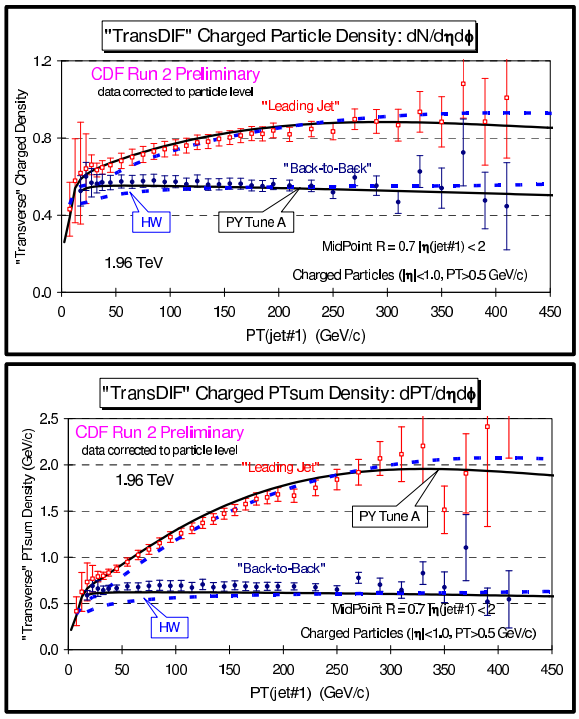

Fig. 26. CDF Run 2 data at 1.96 TeV on the density of charged particles, $dN/d\eta d\phi$ (top), and the charged $p_{\rm T}$ sum density, $dp_{\rm T}/d\eta d\phi$ (bottom), with $p_{\rm T} > 0.5\,{\rm GeV}/c$ and $|\eta| < 1$ for "transMAX" minus "transMIN" for "leading jet" and "back-to-back" events as defined in Fig. 23 as a function of the leading jet $p_{\rm T}$ compared with PYTHIA Tune A and HERWIG. The data are corrected to the particle level (with errors that include both the statistical error and the systematic uncertainty) and compared with the theory at the particle level (*i.e.* generator level).

with PYTHIA Tune A and HERWIG in Fig. 28. Both PYTHIA Tune A and HERWIG lie below the data, but PYTHIA Tune A does a much better job that HERWIG. HERWIG (without multiple parton interactions) predicts a "softer" $p_{\rm T}$ distribution of charged particles than is seen in the data.

As illustrated in Fig. 29, Drell–Yan lepton-pair production provides an excellent place to study the underlying event. Here one studies the outgoing charged particles (excluding the lepton pair) as a function of the lepton-pair invariant mass. After removing the lepton-pair everything else results from the beam–beam remnants, multiple parton interactions, and initial-state radiation. Unlike high $p_{\rm T}$ jet production for lepton-pair production there is no final-state gluon radiation.

Fig. 30 shows that PYTHIA Tune A does not fit the CDF Run 1 Z-boson $p_{\rm T}$ distribution [15]. PYTHIA Tune A was determined by fitting the Run 1 "underlying event" data and, at that time, we did not consider the

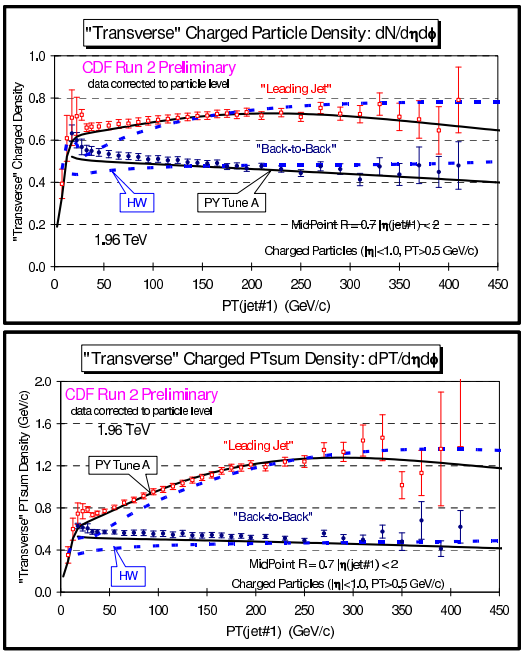

Fig. 27. CDF Run 2 data at 1.96 TeV on the density of charged particles, $dN/d\eta d\phi$ (top), and the charged p_{T} sum density, $dp_{\mathrm{T}}/d\eta d\phi$ (bottom), with $p_{\mathrm{T}} > 0.5\,\mathrm{GeV}/c$ and $|\eta| < 1$ in the overall "transverse" region (average of "transMAX" and "transMIN") for "leading jet" and "back-to-back" events as defined in Fig. 23 as a function of the leading jet p_{T} compared with PYTHIA Tune A and HERWIG. The data are corrected to the particle level (with errors that include both the statistical error and the systematic uncertainty) and compared with the theory at the particle level (*i.e.* generator level).

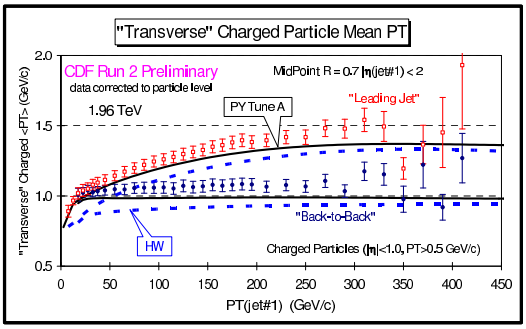

Fig. 28. CDF Run 2 data at 1.96 TeV average p_{T} of charged particles with $p_{\mathrm{T}} > 0.5\,\mathrm{GeV}/c$ and $|\eta| < 1$ in the overall "transverse" region for "leading jet" and "back-to-back" events as defined in Fig. 23 as a function of the leading jet p_{T} compared with PYTHIA Tune A and HERWIG. The data are corrected to the particle level (with errors that include both the statistical error and the systematic uncertainty) and compared with the theory at the particle level (*i.e.* generator level).

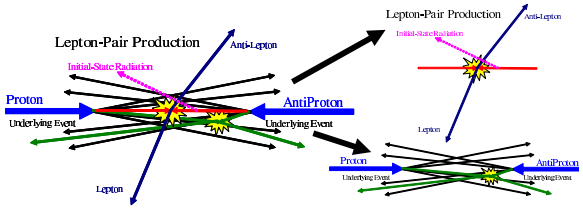

Fig. 29. The "hard scattering" component of the event consists of the two outgoing leptons plus particles that result from initial-state radiation. The "underlying event" consists of particles that arise from the "beam–beam remnants" and from multiple parton interactions.

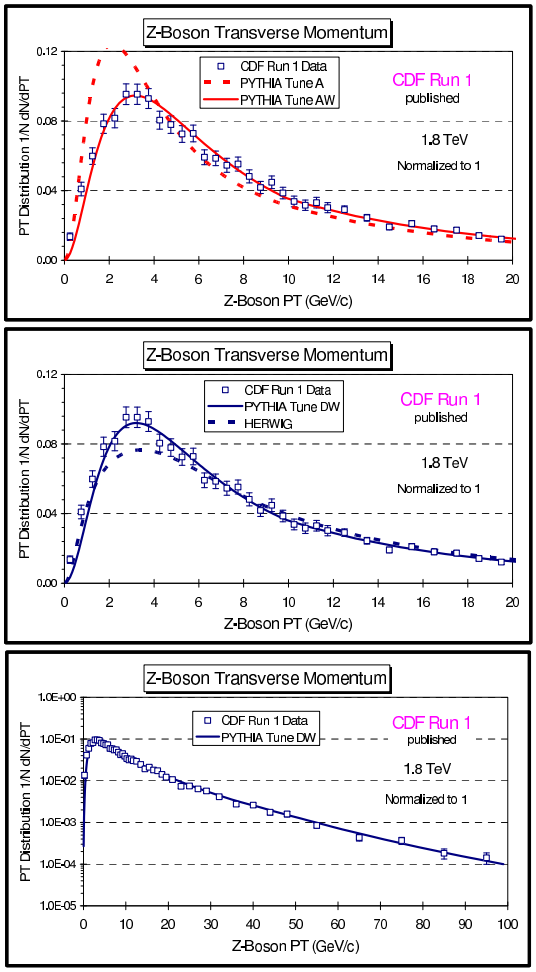

Fig. 30. CDF Run 1 data on the Z-boson p_{T} distribution compared with PYTHIA Tune A, Tune AW, Tune DW, and HERWIG.

Z-boson data. PYTHIA Tune AW fits the Z-boson p_{T} distribution as well as the "underlying event" at the Tevatron [16]. PYTHIA TuneAW is compared with the CDF Run 2 Z-boson p_{T} distribution in Fig. 31. HERWIG

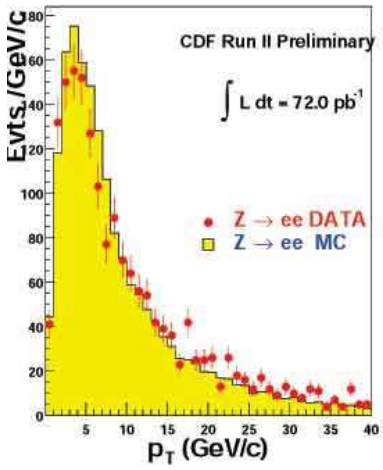

Fig. 31. CDF Run 2 measurement of Z-boson transverse momentum distribution in proton–antiproton collisions at 1.96 TeV with an integrated luminosity of 72 pb^{-1}. The plot shows the shape of the p_{T} distribution of e^+e^- pairs with $67 < M_{ee} < 117$ GeV compared with PYTHIA Tune AW.

does a fairly good job fitting the Z-boson p_{T} distribution without additional tuning, but does not fit the CDF "underlying event" data.

Tables II and III show the parameters for several PYTHIA 6.2 tunes. PYTHIA Tune DW is very similar to Tune AW except PARP(67) = 2.5, which is the preferred value determined by DØ in fitting their di-jet $\Delta\phi$ distribution shown in Fig. 32 [17]. PARP(67) sets the high p_{T} scale for initial-state radiation in PYTHIA. It determines the maximal parton virtuality allowed in time-like showers. Tune BW is a tune with PARP(67) = 1.0. Tune DW and Tune DWT are identical at 1.96 TeV, but Tune DW and DWT extrapolate differently to the LHC. Tune DWT uses the ATLAS energy dependence, PARP(90) = 0.16, while Tune DW uses the Tune A value of PARP(90) = 0.25. All the tunes except Tune D6 use CTEQ5L. Tune D6 and D6T use CTEQ6L. The first 9 parameters in Table II tune the multiple parton interactions (MPI). PARP(62), PARP(62), and PARP(62) tune the initial-state radiation and the last three parameters set the intrinsic k_{T} of the partons within the incoming proton and antiproton.

Table IV shows the computed value of the multiple parton scattering cross-section for the various tunes. The multiple parton scattering cross-section (divided by the total inelastic cross-section) determines the average number of multiple parton collisions per event.

TABLE II

Parameters for several PYTHIA 6.2 tunes. Tune A is a CDF Run 1 "underlying event" tune. Tune AW, DW, DW, and D6 are CDF Run 2 tunes which fit the existing Run 2 "underlying event" data and fit the Run 1 Z-boson p_{T} distribution. Tune D6 is vary similar to Tune DW except that it uses CTEQ6L. The first 9 parameters tune the multiple parton interactions. PARP(62), PARP(64), and PARP(67) tune the initial-state radiation and the last three parameters set the intrinsic k_{T} of the partons within the incoming proton and antiproton.

Parameter	Tune A	Tune AW	Tune DW	Tune BW	Tune D6
PDF	CTEQ5L	CTEQ5L	CTEQ5L	CTEQ5L	CTEQ6L
MSTP(81)	1	1	1	1	1
MSTP(82)	4	4	4	4	4
PARP(82)	2.0	2.0	1.9	1.8	1.8
PARP(83)	0.5	0.5	0.5	0.5	0.5
PARP(84)	0.4	0.4	0.4	0.4	0.4
PARP(85)	0.9	0.9	1.0	1.0	1.0
PARP(86)	0.95	0.95	1.0	1.0	1.0
PARP(89)	1800	1800	1800	1800	1800
PARP(90)	0.25	0.25	0.25	0.25	0.25
PARP(62)	1.0	1.25	1.25	1.25	1.25
PARP(64)	1.0	0.2	0.2	0.2	0.2
PARP(67)	4.0	4.0	2.5	1.0	2.5
MSTP(91)	1	1	1	1	1
PARP(91)	1.0	2.1	2.1	2.1	2.1
PARP(93)	5.0	15.0	15.0	15.0	15.0

As can be seen in Fig. 33, PYTHIA Tune AW, BW, DW, and D6 have been adjusted to give similar results for the charged particle density and the p_{T} sum density in the "transverse" region with $p_{\mathrm{T}} > 0.5\,\mathrm{GeV}/c$ and $|\eta| < 1$ for "leading jet" events at 1.96 TeV.

PHYTIA Tune A agrees fairly well with the CDF Run 2 "underlying event" data for "leading jet" events and Tune AW, BW, DW, and D6 roughly agree with Tune A. Fig. 34 shows that PYTHIA Tune A, Tune DW, and the ATLAS PYTHIA Tune predict about the same density of charged particles in the "transverse" region with $p_{\mathrm{T}} > 0.5\,\mathrm{GeV}/c$ for "leading jet" events at the Tevatron. However, both HERWIG (without MPI) and the ATLAS Tune has a much softer p_{T} distribution of charged particles resulting in a much smaller average p_{T} per particles. Fig. 35 shows that the softer p_{T} distribution of the ATLAS Tune does not agree with the CDF "leading jet" data from Fig. 28.

TABLE III

Parameters for several PYTHIA 6.2 tunes. Tune DWT is identical to Tune DW at 1.96 TeV and Tune D6T is identical to Tune D6 at 1.96 TeV. The ATLAS Tune is the default tune currently used by ATLAS at the LHC. Tune DWT and Tune D6T use the ATLAS energy dependence for the MPI, PARP(90).

Parameter	Tune DWT	ATLAS	Tune D6T
PDF	CTEQ5L	CTEQ5L	CTEQ6L
MSTP(81)	1	1	1
MSTP(82)	4	4	4
PARP(82)	1.9409	1.8	1.8387
PARP(83)	0.5	0.5	0.5
PARP(84)	0.4	0.5	0.4
PARP(85)	1.0	0.33	1.0
PARP(86)	1.0	0.66	1.0
PARP(89)	1960	1000	1960
PARP(90)	0.16	0.16	0.16
PARP(62)	1.25	1.0	1.25
PARP(64)	0.2	1.0	0.2
PARP(67)	2.5	1.0	2.5
MSTP(91)	1	1	1
PARP(91)	2.1	1.0	2.1
PARP(93)	15.0	5.0	15.0

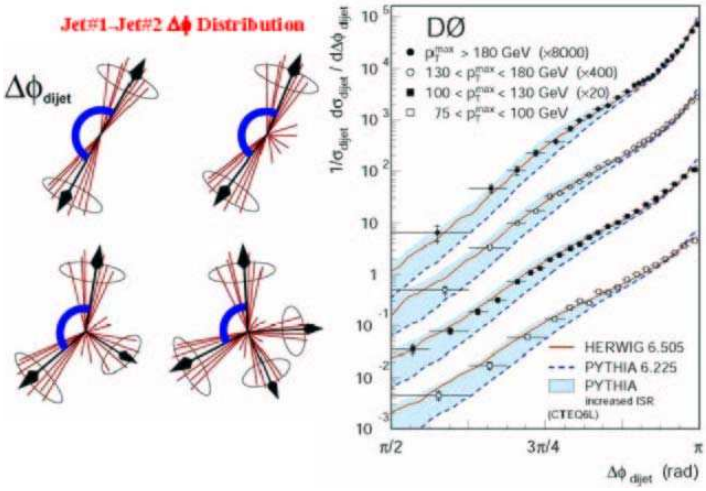

Fig. 32. Shows the DØ Run 2 jet#1-jet#2 $\Delta\phi$ distribution at 1.96 TeV compared with PYTHIA (default) and PYTHIA Tune A (upper edge of the shaded regions). jet#1 and jet#2 are the leading two jets (MidPoint algorithm, $R = 0.7$, $f_{\mathrm{merge}} = 0.5$). The best PYTHIA fit to this data is with PARP(67) = 2.5.

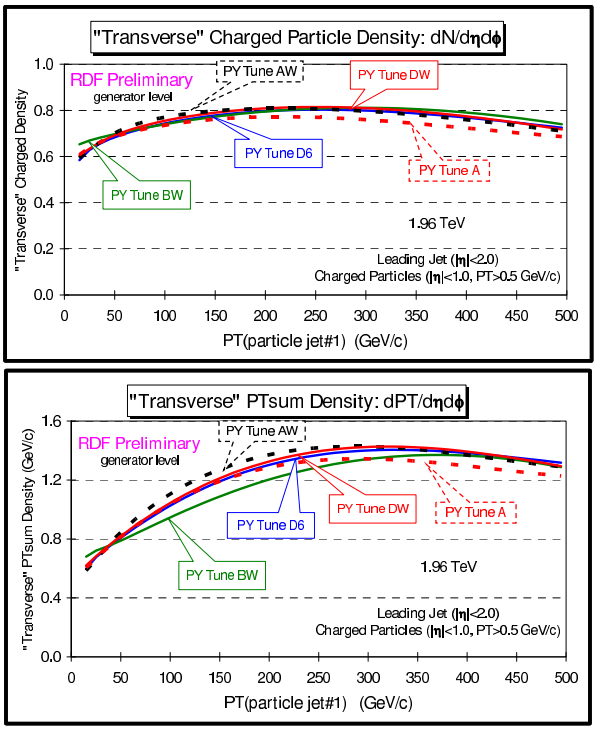

Fig. 33. Predictions at 1.96 TeV of PYTHIA Tune A, Tune AW, Tune BW, Tune DW, and Tune D6 for the density of charged particles, $dN/d\eta d\phi$ (top), and the charged $p_{\rm T}$ sum density, $dp_{\rm T}/d\eta d\phi$ (bottom), with $p_{\rm T} > 0.5$ GeV/c and $|\eta| < 1$ in the overall "transverse" region for "leading jet" events as defined in Fig. 23 as a function of the leading jet $p_{\rm T}$.

TABLE IV

Shows the computed value of the multiple parton scattering cross-section for the various PYTHIA 6.2 tunes.

Tune	σ(MPI) at 1.96 TeV	σ(MPI) at 14 TeV
A, AW	309.7 mb	484.0 mb
DW	351.7 mb	549.2 mb
DWT	351.7 mb	829.1 mb
BW	401.7 mb	624.8 mb
D6	306.3 mb	546.1 mb
D6T	306.3 mb	786.5 mb
ATLAS	324.5 mb	768.0 mb

Fig. 36 shows new data from CDF at 1.96 TeV on the density of charged particles, $dN/d\eta d\phi$, with $p_{\rm T} > 0.5\,{\rm GeV}/c$ and $|\eta| < 1$ for "Leading Jet" and

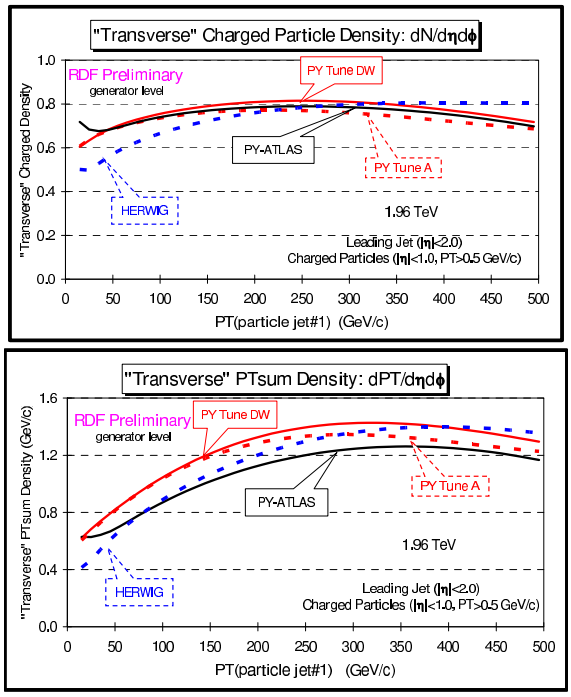

Fig. 34. Predictions at 1.96 TeV of PYTHIA Tune DW (DWT), HERWIG, and the ATLAS Tune for the density of charged particles, $dN/d\eta d\phi$ (top), and the charged p_{T} sum density, $dp_{\mathrm{T}}/d\eta d\phi$ (bottom), with $p_{\mathrm{T}} > 0.5\,\mathrm{GeV}/c$ and $|\eta| < 1$ in the overall "transverse" region for "leading jet" events as defined in Fig. 23 as a function of the leading jet p_{T}. Tune DW and DWT are identical at 1.96 TeV.

"Z-boson" events as a function of the leading jet p_{T} and p_{T}(Z), respectively, for the "toward", "away", and "transverse" regions as defined in Fig. 37. The data are corrected to the particle level and are compared with PYTHIA Tune A and Tune AW, respectively, at the particle level (*i.e.* generator level). Fig. 38 shows the scalar p_{T} sumdensity. For the Z-boson events both the "toward" and "transverse" regions are very sensitive to the "underlying event".

Figs. 39 and 40 compare the "Z-boson" data in the "towards" region with PYTHIA Tune AW, Tune DW, Tune ATLAS, HERWIG (without MPI), and a tuned version of HERWIG plus JIMMY (JIM) [18]. JIMMY is a model for adding multiple parton interaction on to HERWIG. It is not possible to simultaneously fit both the "towards" changed particle density and the "towards" p_{T} sum density with HERWIG plus JIMMY. As can be seen in Fig. 41 HERWIG (without MPI), ATLAS, and HERWIG plus JIMMY all produce p_{T}distributions that as too "soft", whereas the CDF tunes fit the Z-boson data very well.

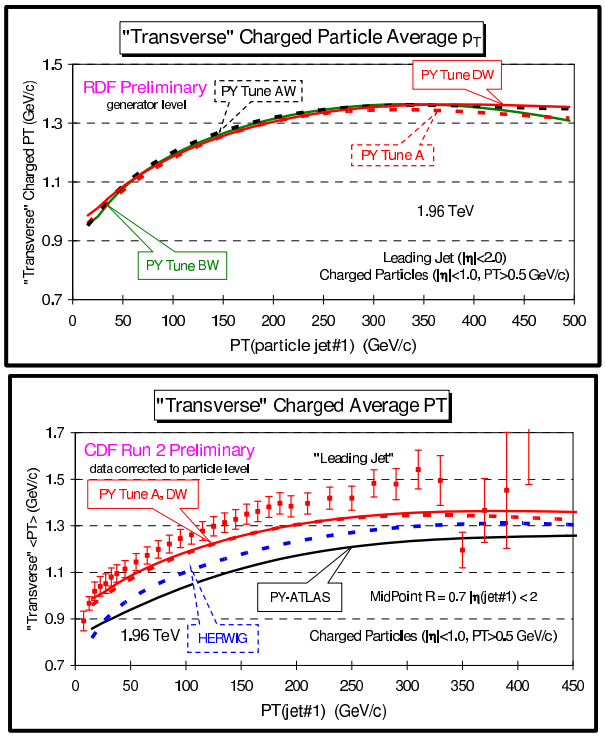

Fig. 35. (Top) Predictions of PYTHIA Tune A, Tune AW, Tune BW, and Tune DW for average p_{T} of charged particles with $p_{\mathrm{T}} > 0.5\,\mathrm{GeV}/c$ and $|\eta| < 1$ in the overall "transverse" region for "leading jet" events at 1.96 TeV as a function of the leading jet p_{T}. (Bottom) CDF Run 2 data at 1.96 TeV on the average p_{T} of charged particles with $p_{\mathrm{T}} > 0.5\,\mathrm{GeV}/c$ and $|\eta| < 1$ in the overall "transverse" region for "leading jet" events as a function of the leading jet p_{T} compared with PYTHIA Tune A, Tune DW, HERWIG, and the ATLAS PYTHIA Tune.

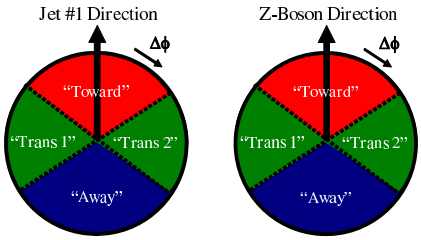

Fig. 36. CDF data at 1.96 TeV on the density of charged particles, $dN/d\eta d\phi$, with $p_{\mathrm{T}} > 0.5\,\mathrm{GeV}/c$ and $|\eta| < 1$ for and "leading jet" (top) and "Z-boson" (bottom) events as a function of the leading jet p_{T} and $p_{\mathrm{T}}(\mathrm{Z})$, respectively, for the "toward", "away", and "transverse" regions. The data are corrected to the particle level (with errors that include both the statistical error and the systematic uncertainty) and are compared with PYTHIA Tune A and Tune AW, respectively, at the particle level (*i.e.* generator level).

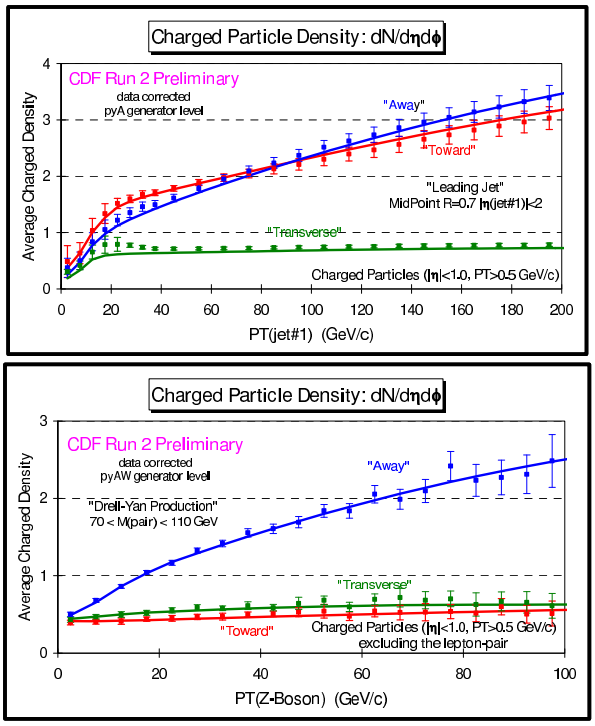

Fig. 37. (Left) illustration of correlations in azimuthal angle $\Delta\phi$ relative to the direction of the leading jet (highest p_{T} jet) in the event, jet#1. The angle $\Delta\phi = \phi - \phi_{\mathrm{jet\#1}}$ is the relative azimuthal angle between charged particles and the direction of jet#1. The "toward" region is defined by $|\Delta\phi| < 60^\circ$ and $|\eta| < 1$, while the "away" region is $|\Delta\phi| > 120^\circ$ and $|\eta| < 1$. The two "transverse" regions $60^\circ < \Delta\phi < 120^\circ$ and $60^\circ < -\Delta\phi < 120^\circ$ are referred to as "transverse 1" and "transverse 2". Each of the two "transverse" regions have an area in $\eta - \phi$ space of $\Delta\eta\Delta\phi = 4\pi/6$. The overall "transverse" region (right) corresponds to combining the "transverse 1" and "transverse 2" regions.

Fig. 42 and Fig. 43 show the extrapolation of PYTHIA Tune DWT and HERWIG (without MPI) for the density of charged particles and the average transverse momentum of charged particles in the "towards" region of Z-boson production to 10 TeV (LHC10) and to 14 TeV (LHC14). For HERWIG (without MPI) the "toward" region of Z-boson production does not change much in going from the Tevatron to the LHC. Models with multiple-parton interactions like PYTHIA Tune DWT predict that the "underlying event" will become much more active (with larger $\langle p_{\mathrm{T}} \rangle$) at the LHC.

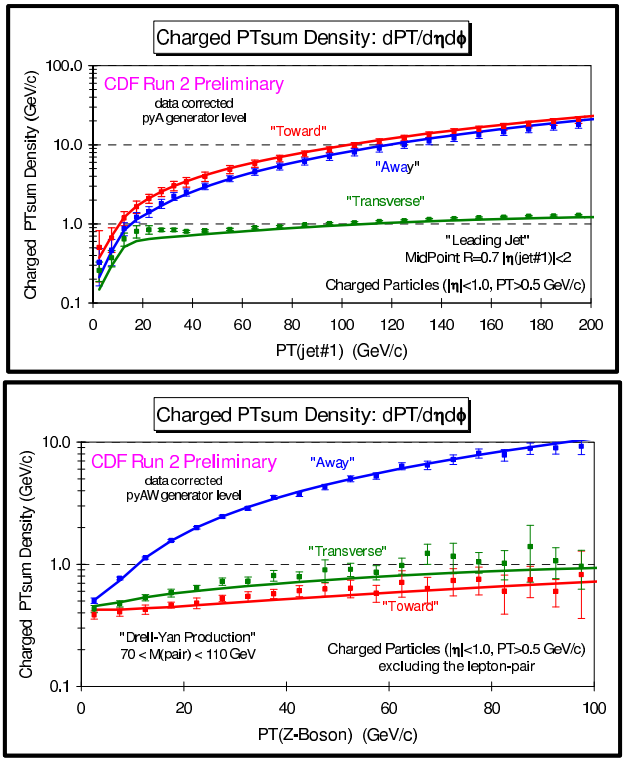

Fig. 38. CDF data at 1.96 TeV on the scalar p_{T} sum density of charged particles, $dp_{\mathrm{T}}/d\eta d\phi$, with $p_{\mathrm{T}} > 0.5\,\mathrm{GeV}/c$ and $|\eta| < 1$ for and "Leading Jet" (top) and "Z-boson" (bottom) events as a function of the leading jet p_{T} and $p_{\mathrm{T}}(\mathrm{Z})$, respectively, for the "toward", "away", and "transverse" regions. The data are corrected to the particle level (with errors that include both the statistical error and the systematic uncertainty) and are compared with PYTHIA Tune A and Tune AW, respectively, at the particle level (*i.e.* generator level).

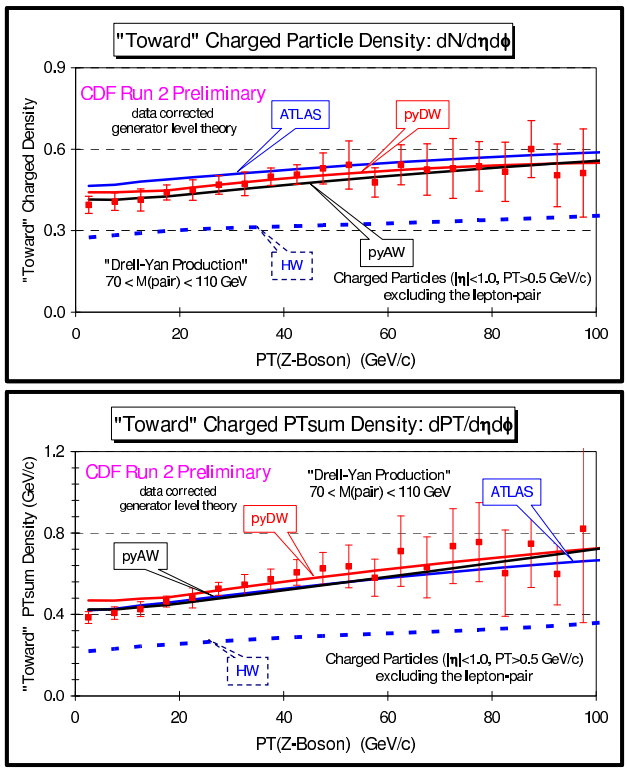

Fig. 39. CDF data at 1.96 TeV on the density of charged particles (top) and the scalar p_{T} sum density (bottom) ($p_{\mathrm{T}} > 0.5\,\mathrm{GeV}/c$, $|\eta| < 1$) for the "towards" region of Z-boson production as a function of $p_{\mathrm{T}}(\mathrm{Z})$. The data are corrected to the particle level and are compared with PYTHIA Tune AW, Tune DW, Tune ATLAS, and HERWIG (without MPI).

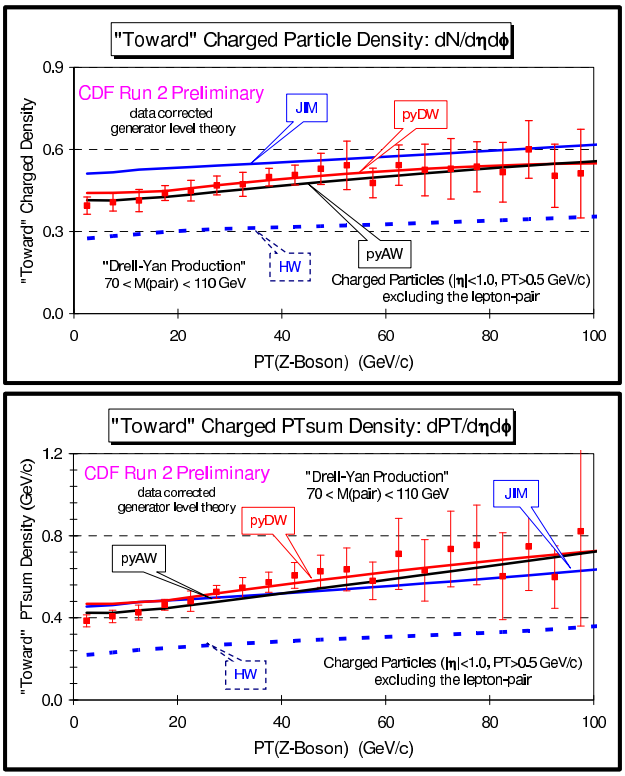

Fig. 40. CDF data at 1.96 TeV on the density of charged particles (top) and the scalar p_T sum density (bottom) ($p_T > 0.5\,\mathrm{GeV}/c$, $|\eta| < 1$) for the "towards" region of Z-boson production as a function of $p_T(Z)$. The data are corrected to the particle level and are compared with PYTHIA Tune AW, Tune DW, HERWIG (without MPI), and a tuned version of HERWIG plus JIMMY (JIM).

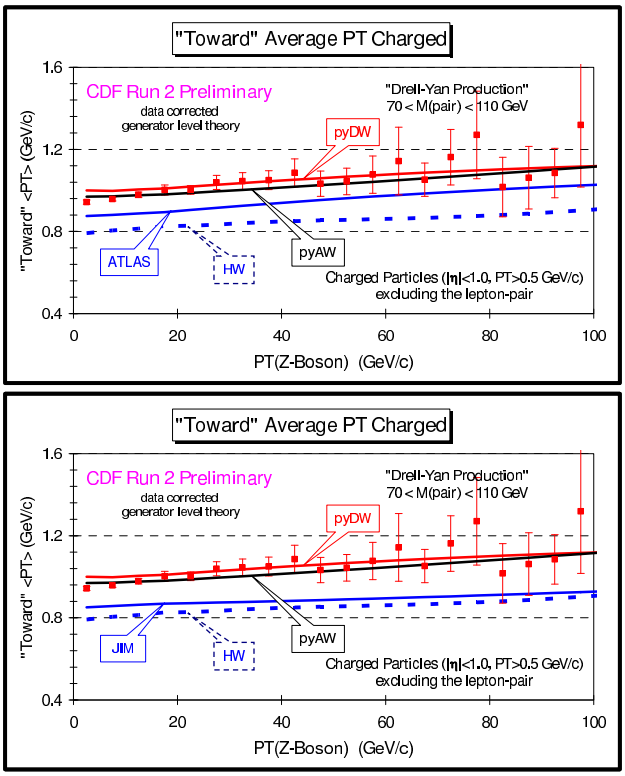

Fig. 41. CDF data at 1.96 TeV on the average transverse momentum of charged particles ($p_{\mathrm{T}} > 0.5\,\mathrm{GeV}/c$, $|\eta| < 1$) for the "towards" region of Z-boson production as a function of $p_{\mathrm{T}}(\mathrm{Z})$. The data are corrected to the particle level and are compared with PYTHIA Tune AW, Tune DW, HERWIG (without MPI), and a tuned version of HERWIG plus JIMMY (JIM).

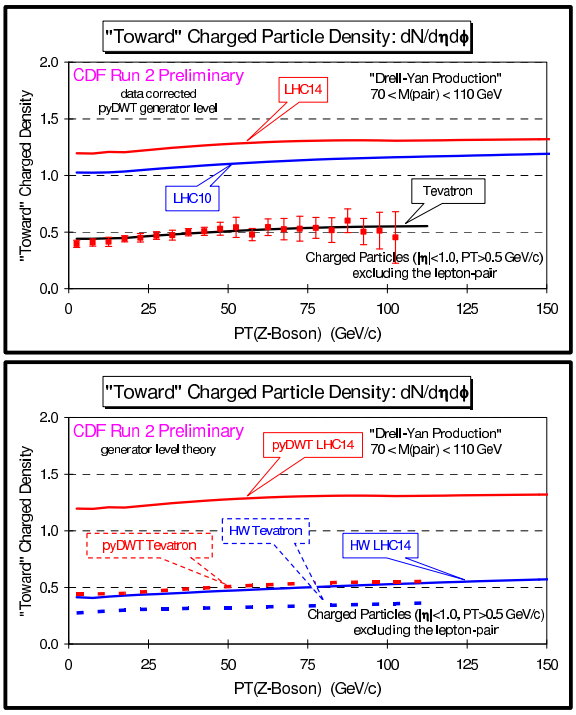

Fig. 42. Shows the predictions of PYTHIA Tune DWT and HERWIG (without MPI) for the density of charged particles ($p_{\mathrm{T}} > 0.5\,\mathrm{GeV}/c$, $|\eta| < 1$) in the "towards" region of Z-boson production as a function of $p_{\mathrm{T}}(\mathrm{Z})$ at 10 TeV (LHC10) and 14 TeV (LHC14).

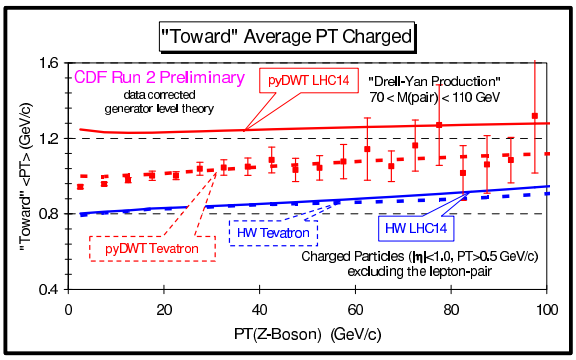

Fig. 43. Shows the predictions of PYTHIA Tune DWT and HERWIG (without MPI) for the average transverse momentum of charged particles ($p_{\mathrm{T}} > 0.5\,\mathrm{GeV}/c$, $|\eta| < 1$) in the "towards" region of Z-boson production as a function of $p_{\mathrm{T}}(\mathrm{Z})$ at 14 TeV (LHC14).

4. Vector boson production

Fig. 44 shows the invariant mass spectrum of $e+e$ pairs near the Z-boson mass and the Z-boson total cross-section measured by CDF. With $72\,\mathrm{pb}^{-1}$ of data CDF has 4242 Z-boson events in the range $67 < M_{ee} < 117\,\mathrm{GeV}$. Fig. 45 shows a summary of the CDF Run 2 measurements of the Z-boson cross-section (times branching fraction) in proton–antiproton collisions at 1.96 TeV for $Z \to e^+e^-$, $Z \to \mu^+\mu^-$, and $Z \to \tau^+\tau^-$ compared with the next-to-next-to-leading order (NNLO) theory prediction. The Z-boson cross-section at the Tevatron agrees well with NNLO theory.

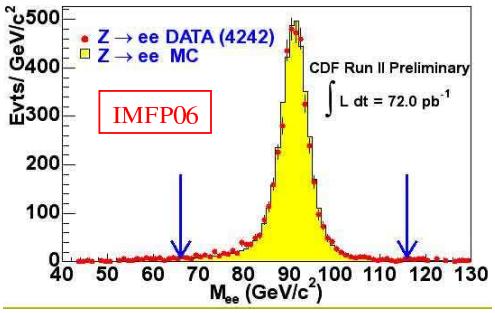

Fig. 44. CDF Run 2 measurement of Z-boson production in proton–antiproton collisions at 1.96 TeV with an integrated luminosity of $72\,\mathrm{pb}^{-1}$. The plot shows the shape of the invariant mass spectrum of $e + e$ pairs with 4242 events in the range $67 < M_{ee} < 117\,\mathrm{GeV}$ compared with PYTHIA Tune AW. The Z-boson cross-section at the Tevatron agrees well with NNLO theory.

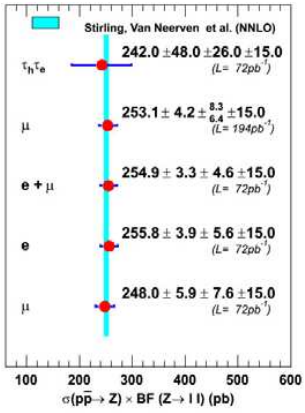

Fig. 45. Summary of the CDF Run 2 measurements of the Z-boson cross-section (times branching fraction) in proton–antiproton collisions at 1.96 TeV for $Z \to e^+e^-$, $Z \to \mu^+\mu^-$, and $Z \to \tau^+\tau^-$ compared with the NNLO theory prediction.

As illustrated in Fig. 46 measurements of the Z-boson at high rapidity probe the high x region of the parton distribution functions.

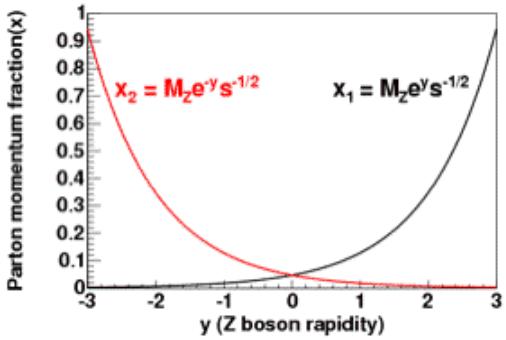

Fig. 46. Parton momentum fractions, x_1 and x_2, as a function of the Z-boson rapidity, $y(Z)$, for Z-boson production in proton–antiproton collisions at 1.96 TeV. Measurements in high $y(Z)$ region probe the high x region of the parton distribution functions.

Fig. 47 shows the electron–positron invariant mass in the region of the Z-boson ($66 < M_Z < 116$ GeV) from CDF Run 2 with 1.1 fb^{-1} of data. This analysis is new since IMFP06 and uses electrons measured in both the central and plug calorimeter yielding a total of 91,362 Z-boson events. Fig. 48 shows the resulting Z-boson rapidity distribution compared with NLO theory using the CTEQ6.1 parton distribution functions. Fig. 49 shows the ratio of data divided theory for the CDF Z-boson rapidity distribution. This data provides a nice constraint for the parton distribution functions. CTEQ6.1 fits slightly better than MRST.

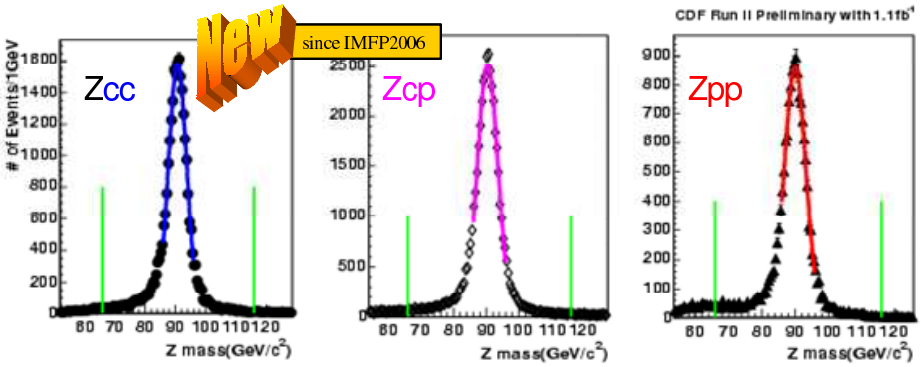

Fig. 47. Electron-positron invariant mass in the region of the Z-boson ($66 < M_Z < 116$ GeV) from CDF Run 2 (1.1 fb^{-1}) of data. This analysis is new since IMFP06 and uses both central (c) and plug electrons (p) resulting in a total of 91,362 Z-boson events.

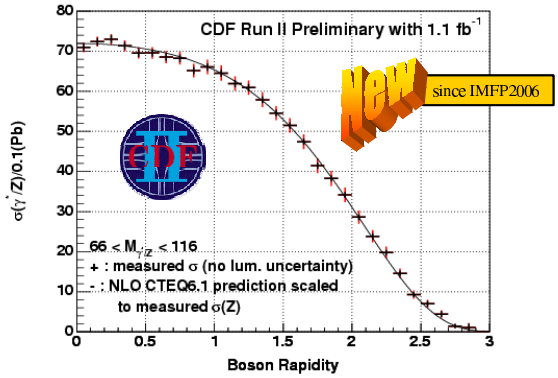

Fig. 48. CDF Run 2 measurement of the Z-boson rapidity distribution in proton–antiproton collisions at 1.96 TeV compared with the NLO theory prediction using CTEQ6.1 (scaled to the measured Z-boson cross-section). This measurement is new since IMFP06.

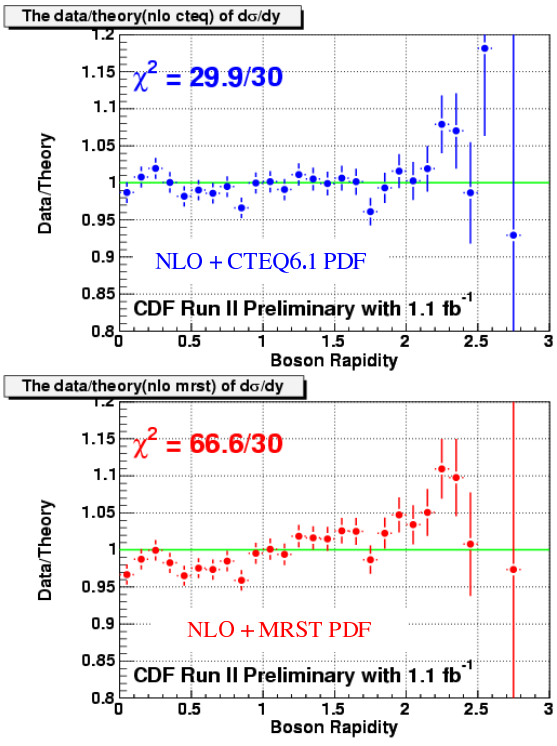

Fig. 49. Shows the ratio of data divided theory for the CDF Z-boson rapidity distribution shown in Fig. 48. The theory is NLO using CTEQ6.1 parton distribution functions (top) and MRST parton distribution functions (bottom).

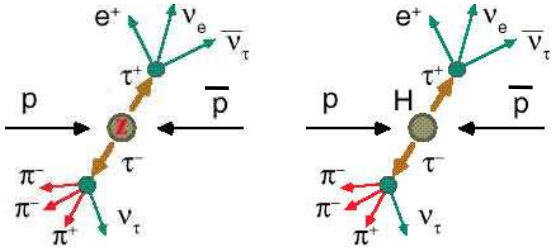

Fig. 50. Shows the production of a Z-boson (left) or a Higgs-boson (right) in proton–antiproton collisions in which the Z-boson (or Higgs-boson) subsequently decays into a $\tau^+\tau^-$ pair where one of the τ's decays hadronically and one decays leptonically.

Both CDF and DØ have worked hard to develop techniques for detecting tau leptons so that they can reconstruct the $\tau^+\tau^-$ invariant mass spectrum. As illustrated in Fig. 50 this allows one not only to see $Z \to \tau^+\tau^-$, but also to search for Higgs $\to \tau^+\tau^-$. Fig. 51 shows the CDF Run 2 measurement of $Z \to \tau^+\tau^-$ production where one of the τ's decays hadronically and one decays leptonically that I showed at IMFP06. The leptonic tau decay is identified by observing the lepton and missing transverse energy. The hadronic tau decay produces a "mini-jet" consisting of a π^0 plus several charged pions. As illustrated in Fig. 52, this cluster of pions is required to be in a 10° cone which is isolated in a 30° cone. CDF uses its Central

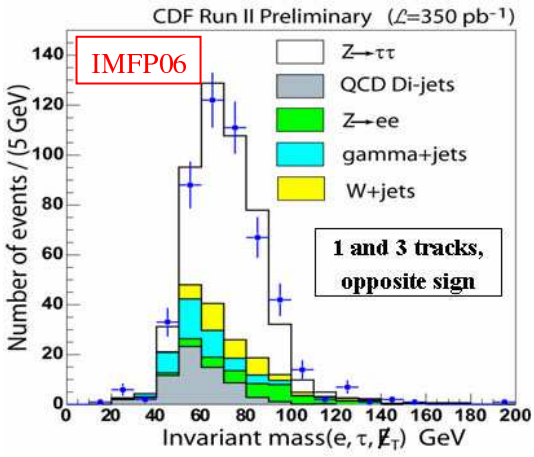

Fig. 51. CDF Run 2 measurement of $Z \to \tau^+\tau^-$ production in proton–antiproton collisions at 1.96 TeV with 316 candidate events with an integrated luminosity of 350 pb^{-1}. The plot shows the shape of the invariant mass spectrum of a τ-lepton reconstructed from its decay into a π^0 plus one or three charged tracks combined with an electron from leptonic decay of a second τ-lepton and the missing energy.

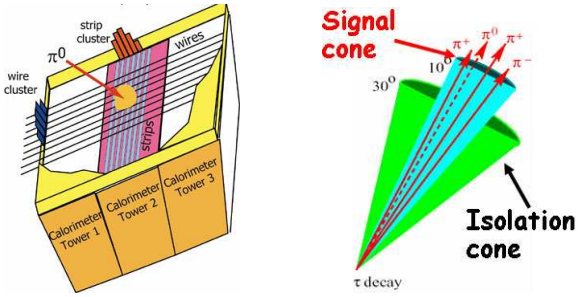

Fig. 52. Left: Illustration of the CDF Central Electron Shower detector (CES). The CES is used to identify π^0's, photons, and electrons. Right: Show the "signal" cone (10°) and the "isolation" cone (30°) used to identify τ-leptons that decay into a "mini-jet" consisting of a π^0 plus several charged pions.

Electron Shower detector (CES) to identify π^0's, photons, and electrons. The CES measures the shape of the shower produced when one of these particles hits the detector. Fig. 53 shows a search for Higgs $\rightarrow \tau^+\tau^-$ at CDF using these techniques with 310 pb^{-1} that I showed at IMFP06 and Fig. 54 shows a more recent CDF Higgs $\rightarrow \tau^+\tau^-$ search with 1.8 fb^{-1} (new since IMFP06).

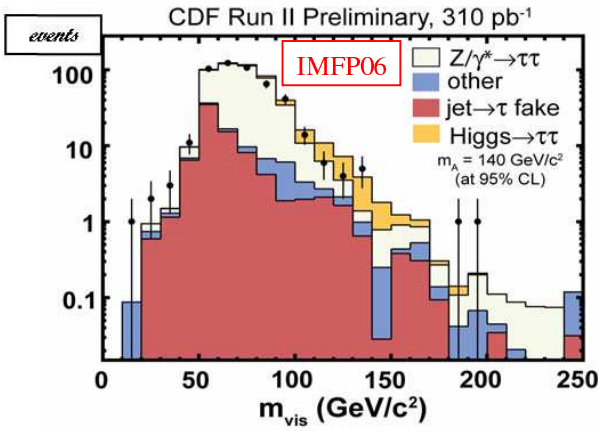

Fig. 53. CDF Run 2 measurement of the shape of the reconstructed $\tau^+\tau^-$ invariant mass spectrum in proton–antiproton collisions at 1.96 TeV with an integrated luminosity of 310 pb^{-1}. The data exclude a 140 GeV/c^2 Higgs $\rightarrow \tau^+\tau^-$ within the MSSM scenario at a 95 % confidence level.

No significant excess of events above Standard Model background is observed resulting in the limits shown in Fig. 55.

Fig. 56 shows a CDF measurement of the W-boson cross-section at the Tevatron with 223 pb^{-1} which uses electron in the forward region of the CDF detector $1.2 < |\eta| < 2.8$.

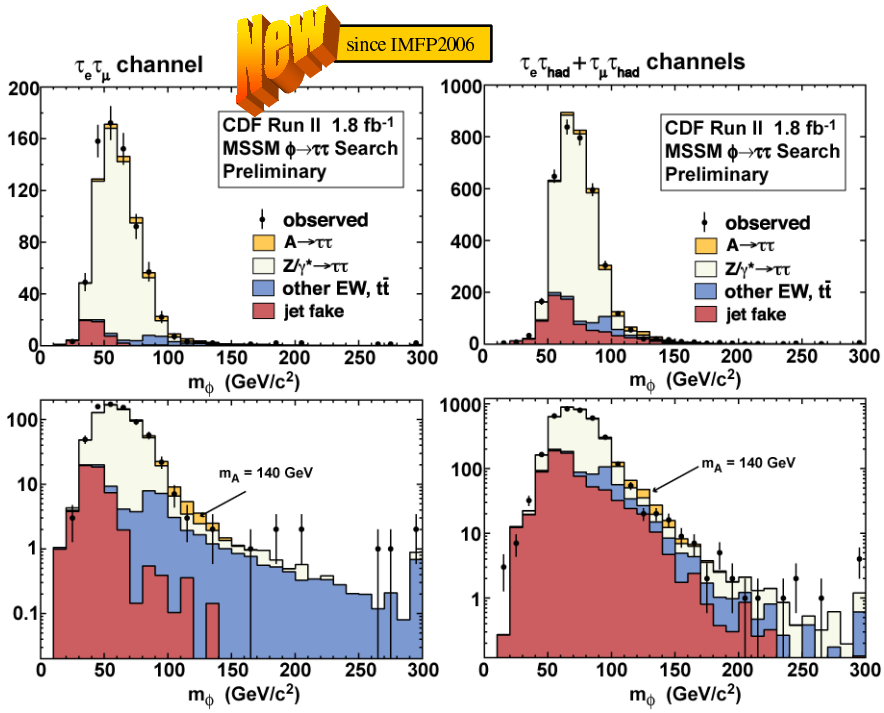

Fig. 54. CDF Run 2 measurement of the shape of the reconstructed $\tau^+\tau^-$ invariant mass spectrum in proton–antiproton collisions at 1.96 TeV with an integrated luminosity of 1.8 fb^{-1}. No significant excess of events above Standard Model background is observed.

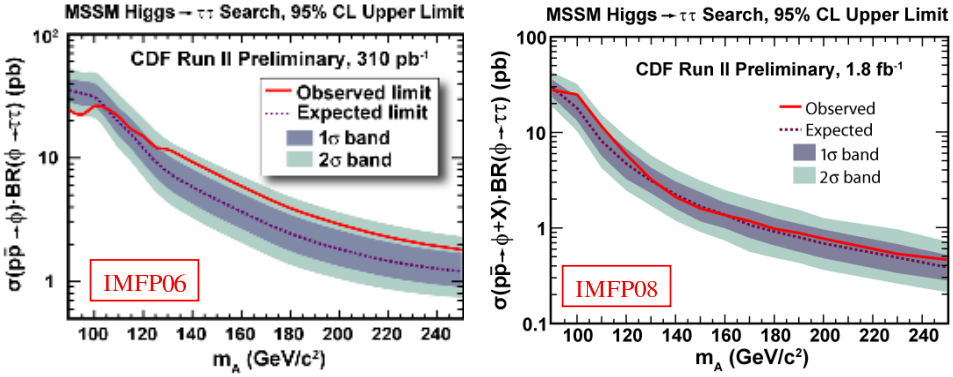

Fig. 55. Shows the CDF Run 2 observed and expected limit on the Higgs mass for Higgs $\to \tau^+\tau^-$ in proton–antiproton collisions at 1.96 TeV with an integrated luminosity of 310 pb^{-1} (IMFP06, left) and with an integrated luminosity of 1.8 fb^{-1} (IMFP08, right).

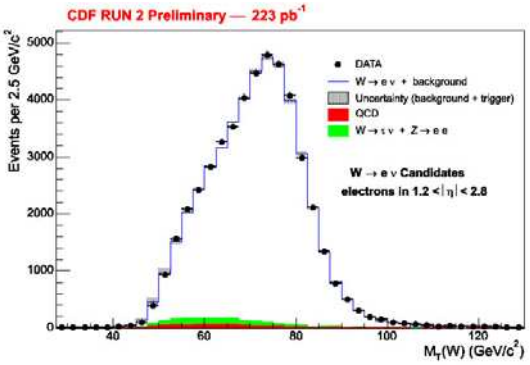

Fig. 56. CDF Run 2 measurement of W-boson production in proton–antiproton collisions at 1.96 TeV with an integrated luminosity of 223 pb^{-1}. There are 48,144 W candidates with a background of about 4.5 %. The plot shows the shape of the transverse mass spectrum constructed from and electron in the forward region of the CDF detector $1.2 < |\eta| < 2.8$ and the missing transverse energy.

Table V compares the forward electron result with the previous measurement which used electrons in the central region of the detector. At the 1.96 TeV the $W \to e\nu$ cross-section is about 11 times larger than the $Z \to e^+e^-$ cross-section. The branching fraction for $Z \to e^+e^-$ is about 3.4 %, whereas the $W \to e\nu$ branching fraction is about 3.2 times larger (about 11 %). Hence, the overall W/Z production ratio is around 3.4 at 1.96 TeV. Fig. 57 shows the recent CDF Run 2 measurement of W-boson mass using an integrated luminosity of 200 pb^{-1}. The measured value of $80.413 \pm 0.048\,\mathrm{GeV}/c^2$ is the most precise measurement of the W-boson mass to date. This measurement is new since IMFP06.

TABLE V

CDF Run 2 results on the cross-section times branching fraction for W and Z bosons in proton–antiproton collisions at 1.96 TeV. The W-boson cross-section is measured using electrons from the central and forward region of the detector. The data are compared with NNLO theory calculations.

	CDF Data (1.96 TeV)	NNLO Theory
$\sigma(Z \to e^+e^-)$	$254.9 \pm 3.3\,(\mathrm{stat}) \pm 4.6\,(\mathrm{sys}) \pm 15.2\,(\mathrm{lum})\,\mathrm{pb}$	$252.3 \pm 5.0\,\mathrm{pb}$
$\sigma(Z \to \tau^+\tau^-)$	$265 \pm 20\,(\mathrm{stat}) \pm 21\,(\mathrm{sys}) \pm 15\,(\mathrm{lum})\,\mathrm{pb}$	$252.3 \pm 5.0\,\mathrm{pb}$
$\sigma(W \to e\nu)^{\mathrm{forward}}$	$2815 \pm 13\,(\mathrm{stat}) \pm 94\,(\mathrm{sys}) \pm 169\,(\mathrm{lum})\,\mathrm{pb}$	$2687 \pm 54\,\mathrm{pb}$
$\sigma(W \to e\nu)^{\mathrm{central}}$	$2775 \pm 10\,(\mathrm{stat}) \pm 53\,(\mathrm{sys}) \pm 167\,(\mathrm{lum})\,\mathrm{pb}$	$2687 \pm 54\,\mathrm{pb}$
$\frac{\sigma(W \to e\nu)}{\sigma(Z \to e^+e^-)}$	$10.92 \pm 0.15\,(\mathrm{stat}) \pm 0.14\,(\mathrm{sys})$	10.69 ± 0.08

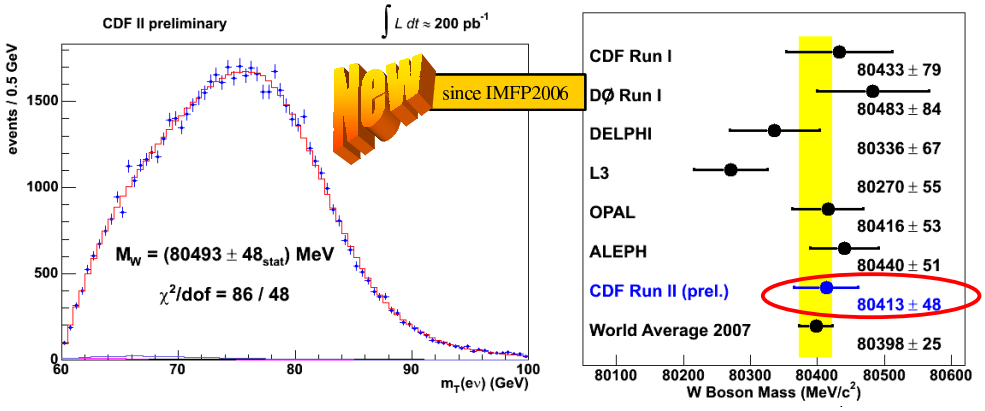

Fig. 57. CDF Run 2 measurement of W-boson mass using an integrated luminosity of 200 pb^{-1}. The measured value of 80.413±0.048 GeV/c^2 is the most precise measurement of the W-boson mass to date. This measurement is new since IMFP06.

There are more u-quarks than d-quarks at high x in the proton and hence the produced W^+ is boosted in the direction of the incoming proton and the W^- is boosted in the direction of the incoming antiproton in proton–antiproton collisions as illustrated in Fig. 58. Fig. 59 shows the recent CDF Run 2 measurement of W-boson production charge asymmetry with an integrated luminosity of 1 fb^{-1} compared with NNLO theory.

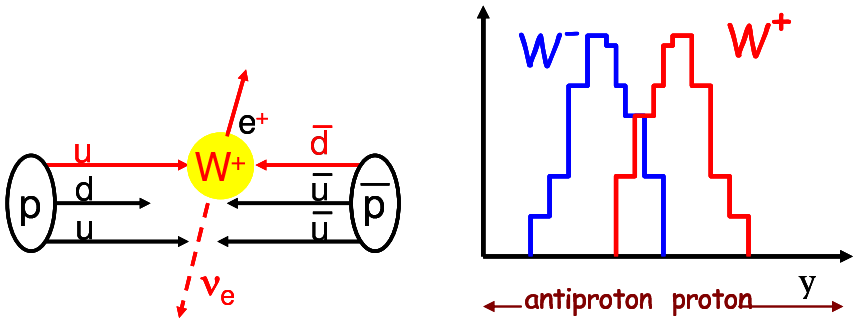

Fig. 58. There are more u-quarks than d-quarks at high x in the proton and hence the produced W^+ (W^-) is boosted in the direction of the incoming proton (antiproton) in proton–antiproton collisions.

Both CDF and DØ are measuring the rate of producing two vector bosons at the Tevatron (*i.e.* di-boson production). The leading order Feynman diagrams for producing $W+\gamma$ and $Z+\gamma$ in proton–antiproton collisions are shown in Fig. 60, Fig. 61 and Fig. 62 shows the CDF data with 202 pb^{-1} and with 1 fb^{-1}, respectively.

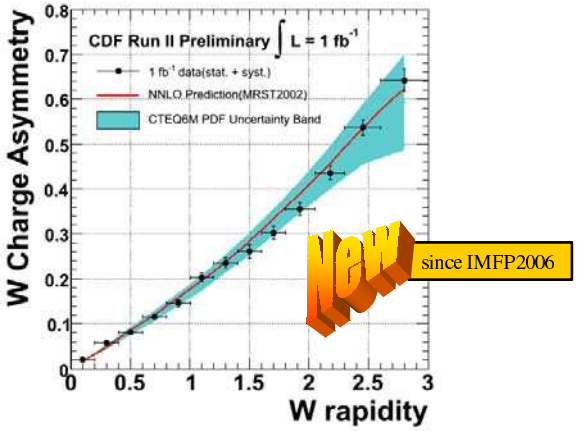

Fig. 59. CDF Run 2 measurement of W-boson production charge asymmetry in proton–antiproton collisions at 1.96 TeV with an integrated luminosity of 1 fb^{-1} compared with NNLO theory (MRST2002). The charge asymmetry is defined by $A(y_W) = (d\sigma^+/dy_W - d\sigma^-/dy_W)/(d\sigma^+/dy_W + d\sigma^-/dy_W)$.

Table VI compares the measured cross-sections with the NLO theory predictions. Note that at 1.96 TeV $\sigma(W)/\sigma(Z) \approx 3.4$ while $\sigma(W+g)/\sigma(Z+g) \approx 1.2$! This is an interesting quantum mechanical effect due to the fact that the s-channel amplitude in Fig. 60 is absent for $Z+\gamma$ production. For $W+\gamma$ production the s-channel amplitude interferes destructively with the t and u-channel amplitudes which suppresses $W+\gamma$ production relative to $Z+\gamma$ production.

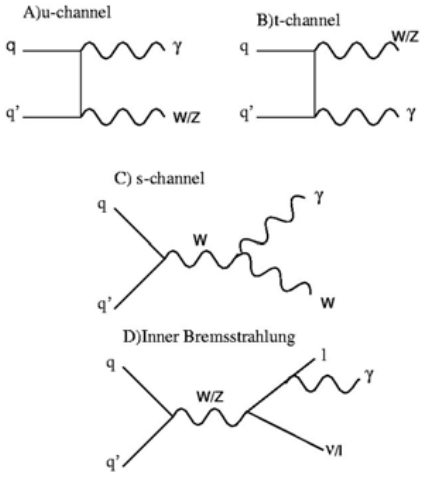

Fig. 60. Leading order Feynman diagrams for producing $W+\gamma$ and $Z+\gamma$ in proton–antiproton collisions.

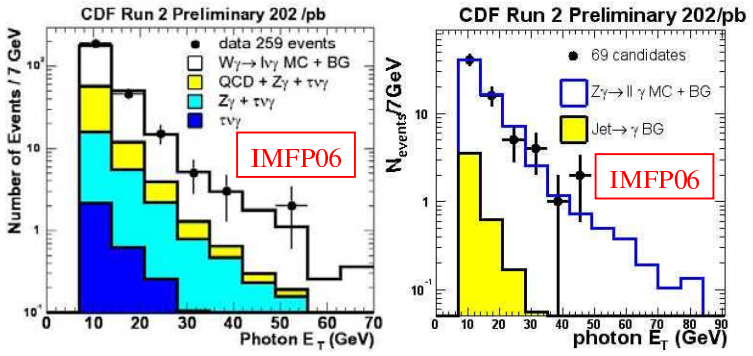

Fig. 61. CDF Run 2 measurement of $W + \gamma$ (259 events, left) and $Z + \gamma$ (69 events, right) production in proton–antiproton collisions at 1.96 TeV with an integrated luminosity of 202 pb^{-1} (shown at IMFP06). The plot shows the shape of the photon transverse energy spectrum compared with QCD theory predictions.

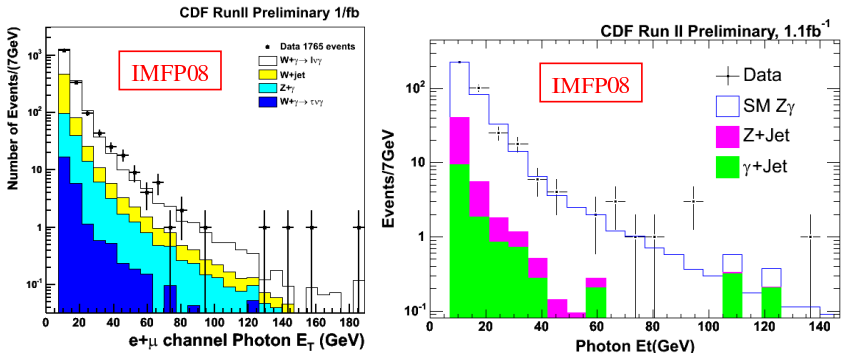

Fig. 62. Recent CDF Run 2 measurement of $W+\gamma$ (1765 events, left) and $Z+\gamma$ (390 events, right) production in proton–antiproton collisions at 1.96 TeV with an integrated luminosity of 1.1 fb^{-1}. The plot shows the shape of the photon transverse energy spectrum compared with QCD theory predictions.

TABLE VI

CDF Run 2 results on the cross-section two vector bosons in proton–antiproton collisions at 1.96 TeV. The W-boson cross-section is measured using electrons from the central and forward region of the detector. The data are compared with NNLO theory calculations.

	CDF data (1.96 TeV)	NLO theory
$\sigma(W+\gamma)\times B_{\mathrm{F}}(W\to l\nu)$	$19.7\pm1.7\,(\mathrm{stat})\,\pm2.0\,(\mathrm{sys})\,\pm1.1\,(\mathrm{lum})\,\mathrm{pb}$	$19.3\pm1.4\,\mathrm{pb}$
$\sigma(Z+\gamma)\times B_{\mathrm{F}}(Z\to ll)$	$5.3\pm0.6\,(\mathrm{stat})\,\pm0.3\,(\mathrm{sys})\,\pm0.3\,(\mathrm{lum})\,\mathrm{pb}$	$5.4\pm0.3\,\mathrm{pb}$
$\sigma(W+W)$ $(825\,\mathrm{pb}^{-1})$	$13.7\pm2.3\,(\mathrm{stat})\,\pm1.6\,(\mathrm{sys})\,\pm1.2\,(\mathrm{lum})\,\mathrm{pb}$	$12.4\pm0.8\,\mathrm{pb}$
$\sigma(W+Z)$ $(825\,\mathrm{pb}^{-1})$	$<6.34\,\mathrm{pb}$ (95 % CL)	$3.7\pm0.1\,\mathrm{pb}$

TABLE VII

Summary of the number of WW events observed by CDF at 1.96 TeV with an integrated luminosity of 825 pb^{-1}. CDF observes 95 WW candidate events with a background of about 37.

Mode	ee	$e\mu$	$\mu\mu$	ll
WW	$12.82 \pm 0.06 \pm 1.06$	$28.82 \pm 0.09 \pm 2.39$	$10.71 \pm 0.05 \pm 0.89$	$52.36 \pm 0.12 \pm 4.35$
Drell–Yan	$4.83 \pm 0.52 \pm 1.26$	$3.56 \pm 0.43 \pm 0.93$	$2.82 \pm 0.37 \pm 0.73$	$11.21 \pm 0.77 \pm 2.91$
$t\bar{t}$	$0.05 \pm 0.01 \pm 0.01$	$0.11 \pm 0.01 \pm 0.01$	$0.04 \pm 0.01 \pm 0.00$	$0.20 \pm 0.01 \pm 0.02$
$WZ + ZZ$	$3.62 \pm 0.02 \pm 0.36$	$0.93 \pm 0.01 \pm 0.09$	$3.39 \pm 0.01 \pm 0.34$	$7.93 \pm 0.02 \pm 0.79$
$W\gamma$	$3.57 \pm 0.12 \pm 0.71$	$3.25 \pm 0.10 \pm 0.65$	$0.02 \pm 0.01 \pm 0.00$	$6.83 \pm 0.16 \pm 1.37$
W + jets	$2.96 \pm 0.23 \pm 0.71$	$6.69 \pm 0.41 \pm 1.98$	$1.33 \pm 0.17 \pm 0.53$	$10.99 \pm 0.50 \pm 3.20$
Sum Bkg	$15.03 \pm 0.58 \pm 1.65$	$14.54 \pm 0.60 \pm 2.28$	$7.60 \pm 0.41 \pm 0.97$	$37.16 \pm 0.93 \pm 4.61$
Expected	$28 \pm 0.59 \pm 1.96$	$43 \pm 0.61 \pm 3.31$	$18 \pm 0.41 \pm 1.31$	$90 \pm 0.94 \pm 6.33$
Data	29	47	19	95

The $W + W$ cross-section at the Tevatron is predicted to be about 12 pb. Table VII is a summary of the number of WW events observed by CDF at 1.96 TeV with an integrated luminosity of 825 pb^{-1}. CDF observes 95 WW candidate events with a background of about 37 which yields the cross-section given in Table VI. Fig. 63 shows a comparison of the WW cross-section measurements with the NLO theory predictions. The data agree well with the NLO theory prediction. There are now enough WW events to begin to look at the details of WW production.

Fig. 64 shows the CDF search for $W+Z$ events in a data sample with an integrated luminosity of 825 pb^{-1} I presented at IMFP06. Fig. 65 shows the recent CDF Run 2 measurement (since IMFP06) of $W + Z$ production in proton–antiproton collisions at 1.96 TeV with an integrated luminosity of 1.9 fb^{-1}.

The signal corresponds to three leptons plus missing transverse energy (MET) and the plot shows the lepton pair invariant mass. The signal region shows 22 candidate events with a background of about 5 resulting in a $W+Z$ cross-section of $\sigma(W + Z) = 4.3 \pm 1.3$ (stat) ± 0.2 (sys) ± 0.3 (lum) pb (3.0σ significance). The NLO theory gives $\sigma(W + Z) = 3.7 \pm 0.3$ pb.

Fig. 66 shows the recent CDF Run 2 measurement (since IMFP06) of $Z+Z$ production in proton–antiproton collisions at 1.96 TeV with an integrated luminosity of 1.1 fb^{-1}. The signal corresponds to either four leptons or 2 leptons plus missing transverse energy (MET) and the plot shows the logarithm of the likelihood ratio, $\mathrm{P}_{ZZ}/(\mathrm{P}_{ZZ}+\mathrm{P}_{WW})$. The analysis measures a $Z+Z$ cross-section of $\sigma(Z+Z) = 0.75+0.71-0.54$ pb ($3.0\ \sigma$ significance).

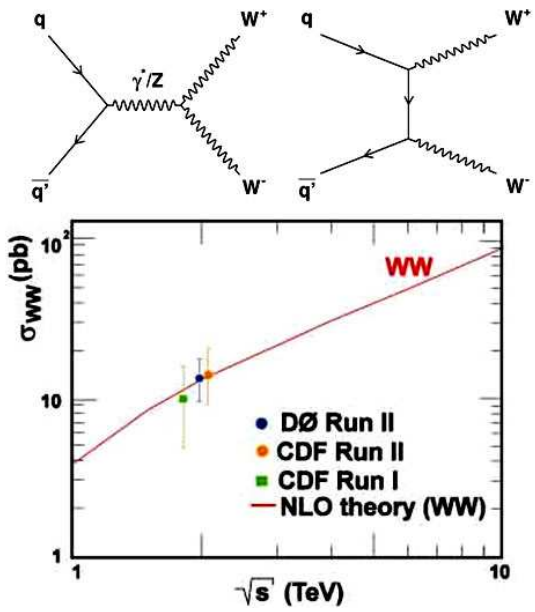

Fig. 63. (Top) leading order Feynman diagrams for $W+W$ production at the Tevatron. (Bottom) comparison of Tevatron measurements for the cross-section of $W+W$ production with the NLO theory predictions.

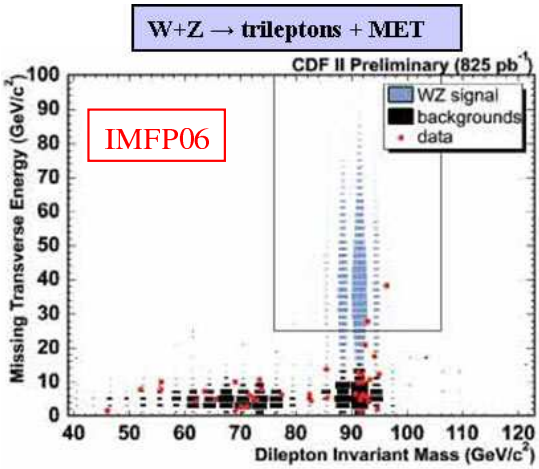

Fig. 64. CDF Run 2 search for $W+Z$ production in proton–antiproton collisions at 1.96 TeV with an integrated luminosity of 825 pb^{-1} (shown at IMFP06). The signal corresponds to three leptons plus missing transverse energy (MET) and the plot shows the MET versus the invariant mass of the lepton-pairs. The signal region (rectangular box) shows 2 candidate events with a background of 0.9 ± 0.2.

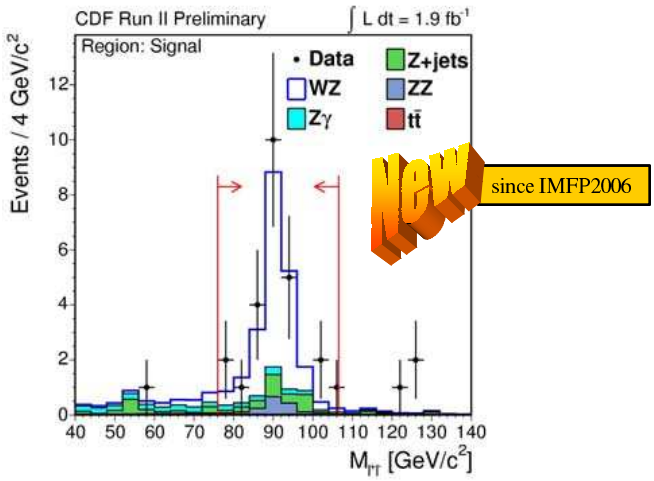

Fig. 65. Recent CDF Run 2 measurement of $W + Z$ production in proton–antiproton collisions at 1.96 TeV with an integrated luminosity of 1.9 fb^{-1}. The signal corresponds to three leptons plus missing transverse energy (MET) and the plot shows the lepton pair invariant mass. The signal region shows 22 candidate events with a background of about 5 resulting in a $W + Z$ cross-section of $\sigma(W + Z) = 4.3 \pm 1.3$ (stat)± 0.2(sys) ± 0.3 (lum) pb (3.0σ significance). The NLO theory gives $\sigma(W + Z) = 3.7 \pm 0.3$ pb.

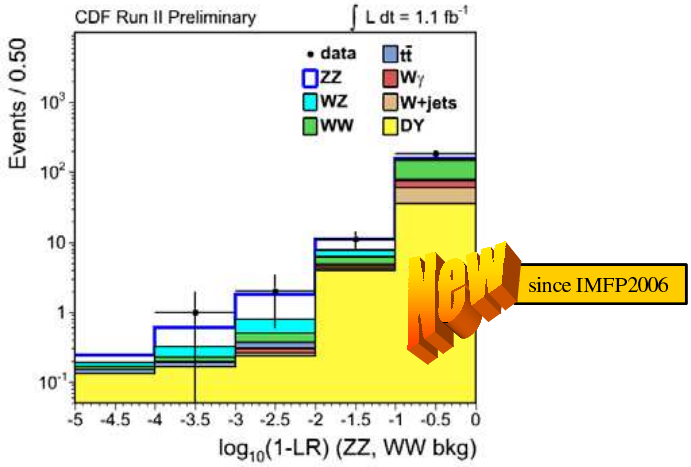

Fig. 66. Recent CDF Run 2 measurement of $Z + Z$ production in proton–antiproton collisions at 1.96 TeV with an integrated luminosity of 1.1 fb^{-1}. The signal corresponds to either four leptons or 2 leptons plus missing transverse energy (MET) and the plot shows the logarithm of the likelihood ratio, $\mathrm{P}_{ZZ}/(\mathrm{P}_{ZZ} + \mathrm{P}_{WW})$. The analysis measures a $Z + Z$ cross-section of $\sigma(Z + Z) = 0.75 + 0.71 - 0.54$ pb (3.0σ significance). The NLO theory gives $\sigma(Z + Z) = 1.4 \pm 0.1$ pb.

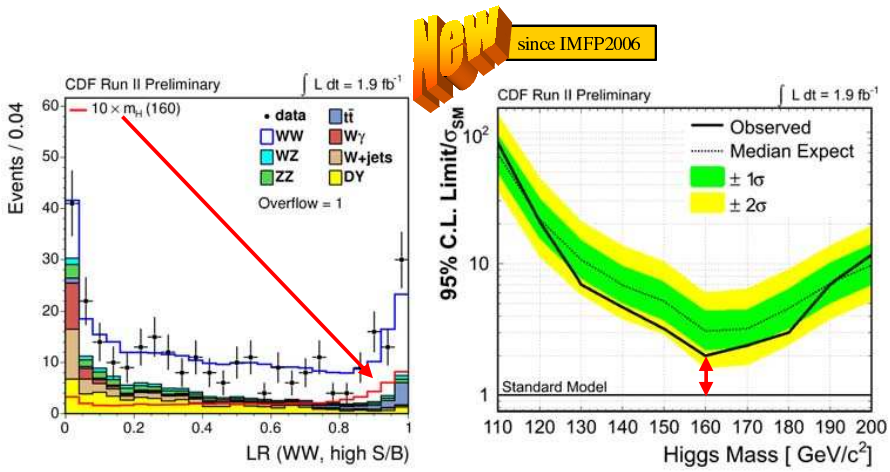

Fig. 67. Recent CDF Run 2 search for Higgs $\rightarrow W+W$ production in proton–antiproton collisions at 1.96 TeV with an integrated luminosity of 1.9 fb^{-1} (left). The CDF limit is within a factor of two of a 160 GeV/c^2 Standard Model Higgs $\rightarrow W+W$ (right).

The NLO theory gives $\sigma(Z+Z) = 1.4 \pm 0.1\,\mathrm{pb}$. At CDF we now have enough $W+W$ events to put fairly strong limits on the Standard Model Higgs $\rightarrow W+W$. Fig. 67 shows the recent CDF Run 2 search for Higgs $\rightarrow W+W$ production in proton–antiproton collisions at 1.96 TeV with an integrated luminosity of 1.9 fb^{-1}. The CDF limit is within a factor of two of a 160 GeV/c^2 Standard Model Higgs $\rightarrow W+W$.

Fig. 68 shows an updated summary of the boson and di-boson measurements at the Tevatron. The W cross-section is around 26 000 pb. About a factor of 3 below the W cross-section is the Z-boson cross-section. About a factor of 40 below the Z-boson cross-section are the $W+\gamma$ and $Z+\gamma$ cross-sections. About a factor of 10 below the $Z+\gamma$ cross-section is the $W+W$ cross-section. About a factor of 3 below the $W+W$ cross-section is the $W+Z$ cross-section and slightly below that is the $Z+Z$ cross-section which CDF has now observed. At the Tevatron we have moved from measuring cross-sections at the 1 000 pb level to measuring cross-sections at the 1 pb level or smaller. The Higgs $\rightarrow W+W$ cross-section might be at the 0.1 pb level. We are getting close! Recent measurements favor a light Higgs mass of around 113GeV. A light Higgs mass is a very interesting scenario for the Tevatron.

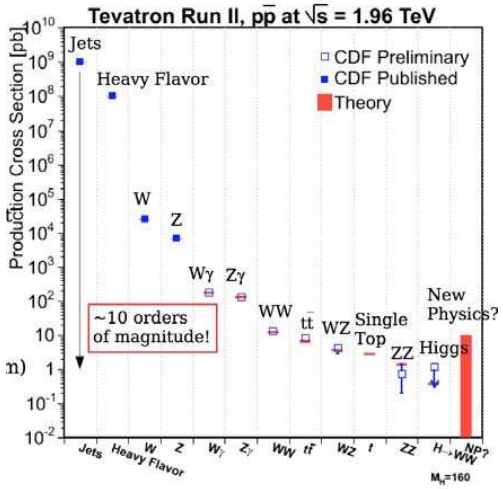

Fig. 68. Summary of the Tevatron measurements (or limits) of the cross-sections for the production of W-bosons, Z-bosons, $W+\gamma$, $Z+\gamma$, $W+W$, $W+Z$, $Z+Z$, and Higgs $\rightarrow W+W$ compared with the Standard Model predictions. CDF and DØ are beginning to measure cross-sections at the 1 pb level and are getting closer to the Higgs.

5. Top quark physics

The top quark was discovered at the Tevatron by CDF and DØ in 1995 and in the last 10 years both experiments have continued to improve on the precision of their measurements. Fig. 69 shows the heavy quark and boson cross-sections for proton–antiproton collisions compared with the total inelastic cross-section at the Tevatron. The top quark cross-section is now measured to an accuracy of about 12% and the top mass is measured to about 2%. At the Tevatron about 15% of the tt pairs are produced by gluon fusion and about 85% from quark–antiquark annihilation. Both CDF and DØ now have hundreds of top quark events and are beginning to study the detailed properties of the top quark (*i.e.* charge, lifetime, branching fractions, *etc.*). The top quark is heavier than a W-boson plus a b-quark so it decays very quickly via the mode $t \rightarrow W + b$. In fact the decay is so rapid that it decays into $W + b$ before it hadronizes. The b-quark fragments into a b-jet and the W-boson decays either leptonically into a lepton and a neutrino (11%) or hadronically into a quark–antiquark pair (67%) resulting in the tt decay channels shown in Fig. 70. The dilepton channel corresponds to both the top and anti-top decaying into a lepton, neutrino, and a b-jet. The lepton+jets channel corresponds to one top quark decaying into a lepton, neutrino, and a b-jet and the other top quark decaying into a b-jet plus two light quark jets. The all jets channel occurs when both top quarks decay into a b-jet plus two light quark jets.

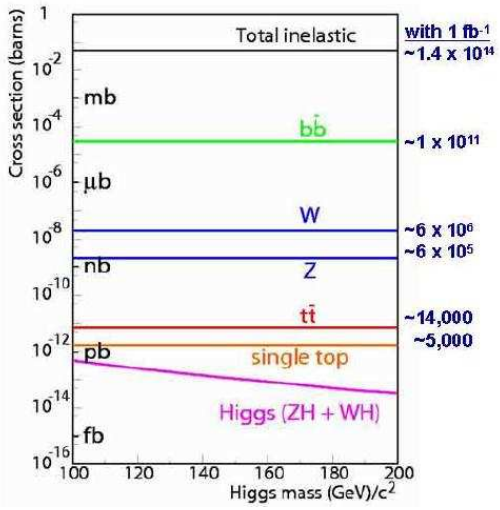

Fig. 69. Heavy quark and Boson cross-sections for proton–antiproton collisions at 1.96 TeV *versus* the Higgs mass compared with the total inelastic cross-section. Also, shown are the number of events produced with 1 fb^{-1} of integrated luminosity.

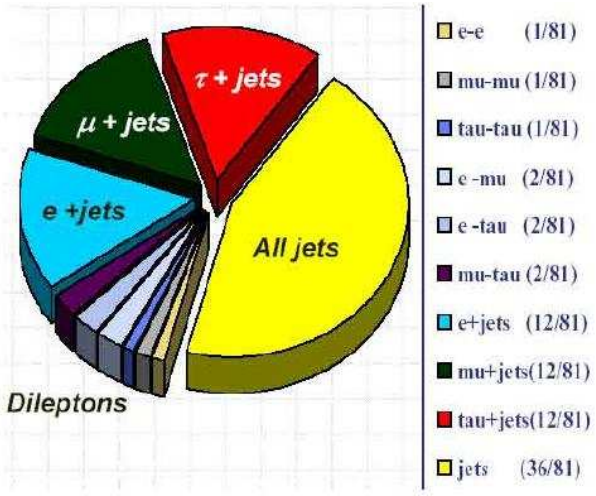

Fig. 70. Pie chart showing decay channels of $t\bar{t}$ quark pairs produced in hadron–hadron collisions.

The smallest cross-section times branching fraction is the dilepton channel. Fig. 71 shows the number of CDF Run 2 $t\bar{t}$ dilepton candidate events in a data sample with an integrated luminosity of 750 pb^{-1} that I presented at IMFP06 and the same plot with an integrated luminosity of 1.2 fb^{-1} (IMFP08). The events are required not to contain a Z-boson and to have two

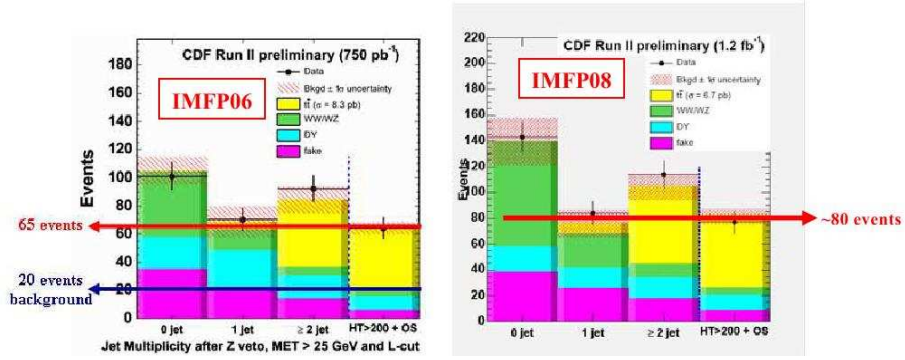

Fig. 71. Shows the number of CDF Run 2 $t\bar{t}$ dilepton candidate events in proton–antiproton collisions at 1.96 TeV in a data sample with an integrated luminosity of 750 pb^{-1} (IMFP06, left) and 1.2 fb^{-1} (IMFP08, right). The events are required not to contain a Z-boson and to have two leptons with $p_{\mathrm{T}} > 20\,\mathrm{GeV}/c$ and missing transverse energy greater than 25 GeV. The plot shows the number of events with 0, 1, and ≥ 2 jets (first three bins). Further requiring ≥ 2 jets, $H_{\mathrm{T}} > 200\,\mathrm{GeV}$, and opposite sign leptons (last bin) yields 80 events with an estimated background of about 25 events and gives a measured tt total cross-section of about 6.2 pb.

leptons with $p_{\mathrm{T}} > 20\,\mathrm{GeV}/c$ and missing transverse energy, MET, greater than 25 GeV. The number of events with opposite sign leptons, and ≥ 2 jets with $E_{\mathrm{T}} > 15\,\mathrm{GeV}$, and $H_{\mathrm{T}} > 200\,\mathrm{GeV}$, has increased from 65 to about 80 events and the resulting tt total cross-section of has changed from about 8.3 pb to 6.7 pb. Note that $H_{\mathrm{T}} = \sum_{\mathrm{leptons}} p_{\mathrm{T}} + \sum_{\mathrm{jets}} E_{\mathrm{T}} + ME_{\mathrm{T}}$.

Fig. 72 shows the number of CDF Run 2 $t\bar{t}$ lepton+jets candidate events in a data sample with an integrated luminosity of 695 pb^{-1} that I presented at IMFP06 and the same plot with an integrated luminosity of 1.12 fb^{-1} (IMFP08).

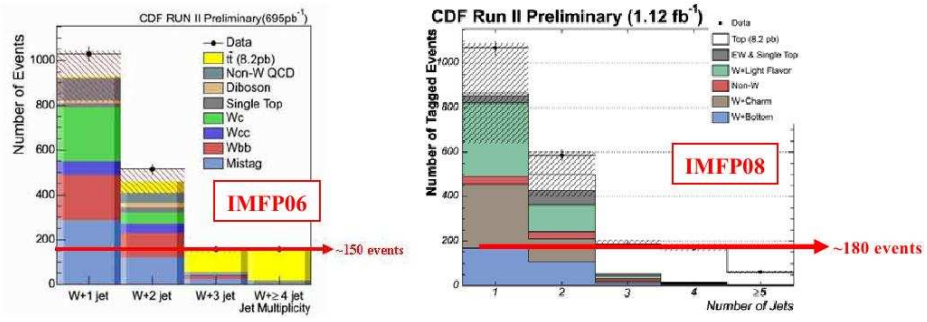

Fig. 72. Shows the number of CDF Run 2 top-quark lepton+jets candidate events in proton–antiproton collisions at 1.96 TeV with an integrated luminosity of 695 pb^{-1} (IMFP06, left) and 1.12 fb^{-1} (IMFP08, right). The events are required to contain a W-boson and to have $H_{\mathrm{T}} > 200\,\mathrm{GeV}$ and to have at least one b-tagged jet. The plot shows the number of events with a W-boson plus 1, 2, 3, and ≥ 4 jets. Requiring $W+ \geq 4$ (last bin) yields about 180 events with a small background resulting in a tt total cross-section of about 8.2 pb.

The events are required to contain a W-boson and to have $H_{\rm T} > 200\,{\rm GeV}$ and to have at least one b-tagged jet. The number of events with $W+ \geq 4$ jets has increased from 150 to around 180 events with a small background resulting in a $t\bar{t}$ total cross-section of about 8.2 pb.

Fig. 73 shows that the number of events with two b-tagged jets and $W+ \geq 4$ jets yields has increased from 45 events to around 70 events with almost no background and gives a $t\bar{t}$ total cross-section of about 8.8 pb. Part of this increase in events is due to the improved b-tagging efficiency at CDF.

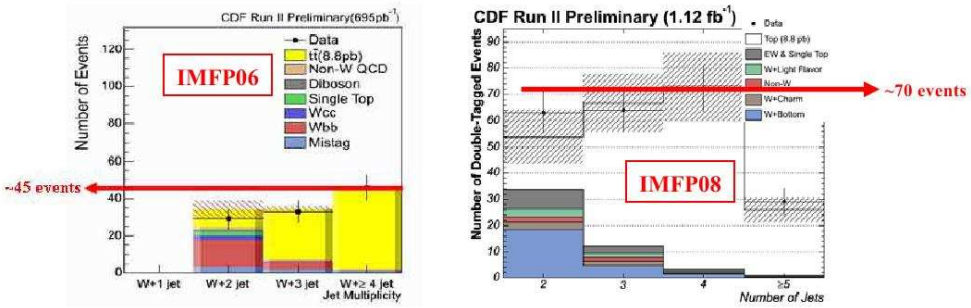

Fig. 73. Shows the number of CDF Run 2 top-quark lepton+jets candidate events in proton–antiproton collisions at 1.96 TeV with an integrated luminosity of 695 $\rm pb^{-1}$ (IMFP06, left) and 1.12 $\rm fb^{-1}$ (IMFP08, right). The events are required to contain a W-boson and to have $H_{\rm T} > 200\,{\rm GeV}$ and to have two b-tagged jets. The plot shows the number of events with a W-boson plus 2, 3, and ≥ 4 jets. Requiring $W+ \geq 4$ jets (last bin) yields about 70 events with almost no background resulting in tt total cross-section of about 8.8 pb.

Fig. 74 and Fig. 75 summarizes the various CDF and DØ Run 2 measurements of the tt total cross-section, respectively, at IMFP06 and today (IMFP08). Fig. 76 summarizes the CDF top mass measurements at IMFP06 and today (IMFP08). Currently the uncertainty on the top quark mass is around 2.8 GeV. CDF expects to eventually achieve an uncertainty of about 1.5 GeV (*i.e.* a 1 % measurement!). Fig. 77 shows the error on the CDF combined total cross-section and top quark mass measurements with the with 760 $\rm pb^{-1}$ (IMFP06) and with 1.2 $\rm fb^{-1}$ (IMFP08). The theory curve is from Cacciari, Mangano, *et al.* [19].

Fig. 78 and Fig. 79 show the CDF search for $t\bar{t}$ resonances.

The Run 1 data and the early Run 2 data show an intriguing structure in the top-pair invariant mass distribution around 500 GeV (*i.e.* an excess of events which might be evidence for a $t\bar{t}$ resonance!). However, this structure has disapeared with the increased statistics.

Top anti-top pairs are produced strongly at the Tevatron with a total cross-section of around 7 pb. Single top quarks are produced weakly with a cross-section of around 2 pb [20]. Fig. 80 shows the sources of single

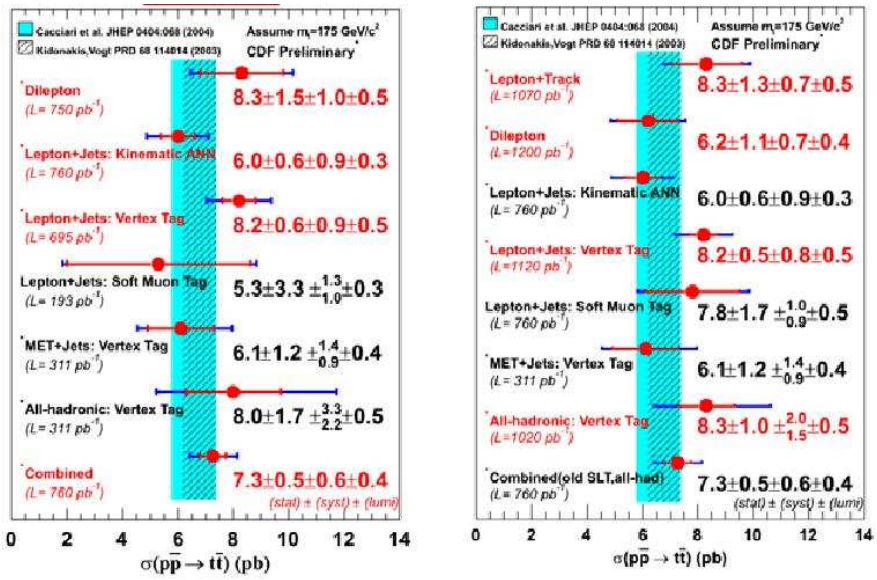

Fig. 74. Summary of CDF Run 2 measurements of the $t\bar{t}$ total cross-section at IMFP06 (left) and IMFP08 (right) assuming a top quark mass of 175 GeV/c^2. The theoretical prediction of $6.7^{+0.7}_{-0.9}$ pb is also shown.

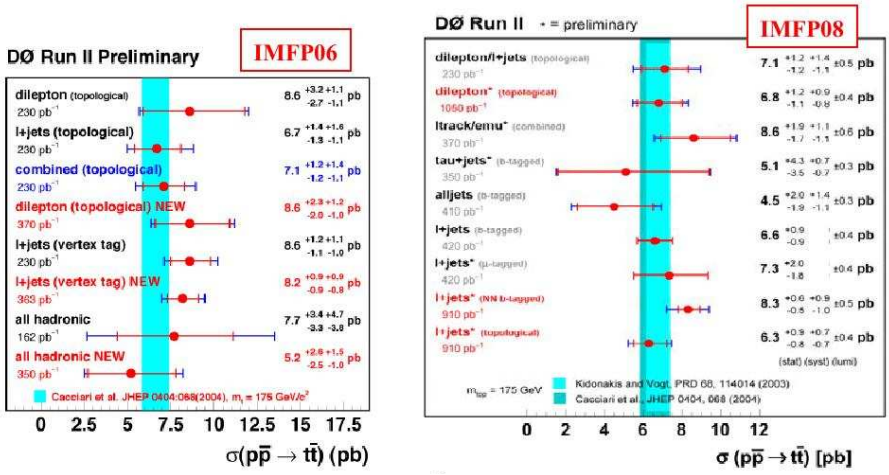

Fig. 75. Summary of DØ Run 2 measurements of the $t\bar{t}$ total cross-section at IMFP06 (left) and IMFP08 (right) assuming a top quark mass of 175 GeV/c^2. The theoretical prediction of $6.7^{+0.7}_{-0.9}$ pb is also shown.

top quark production at the Tevatron. Single top quarks can be produced through s or t-channel W-boson exchange or produced in association with a top quark and a W-boson. Both CDF and DØ have worked very hard to

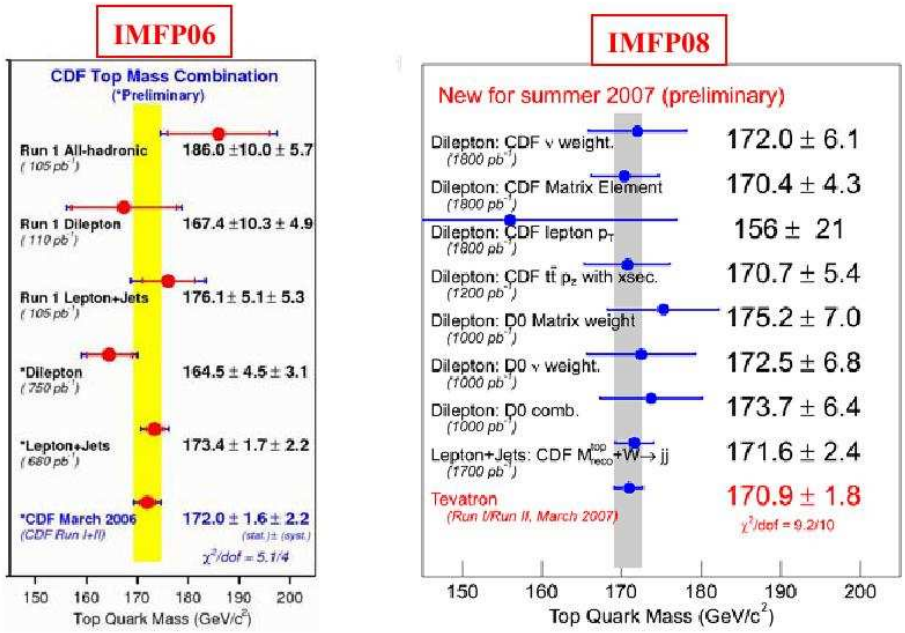

Fig. 76. Summary of various CDF measurements of the top quark mass measurements at IMFP06 (left) and IMFP08 (right).

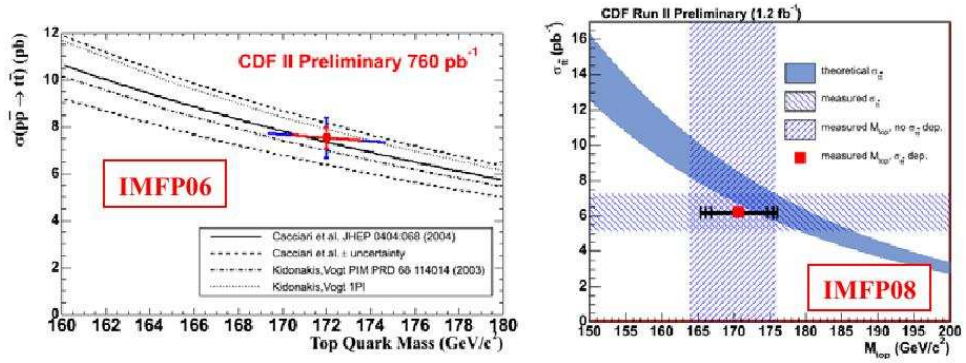

Fig. 77. Shows the error on the CDF combined $t\bar{t}$ total cross-section and top quark mass measurements with 760 pb^{-1} (IMFP06, left) and with 1.2 fb^{-1} (IMFP08, right). The theory curve is from Cacciari, Mangano, *et al.* [19].

observe single top production. At IMFP06 the upper limits were around 3 pb as shown in Fig. 81 and at that time I stated that I thought that single top would soon be discovered at the Tevatron.

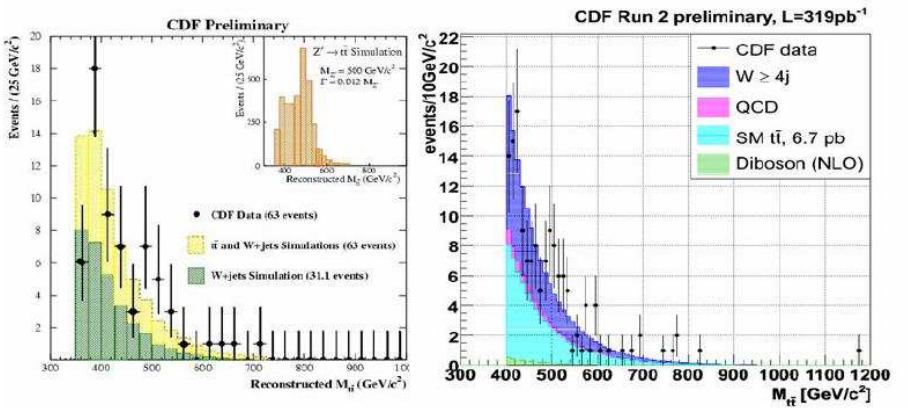

Fig. 78. Shows the CDF $t\bar{t}$ invariant mass distribution from Run 1 (left) and from Run 2 with an integrated luminosity of 319 pb^{-1} (right).

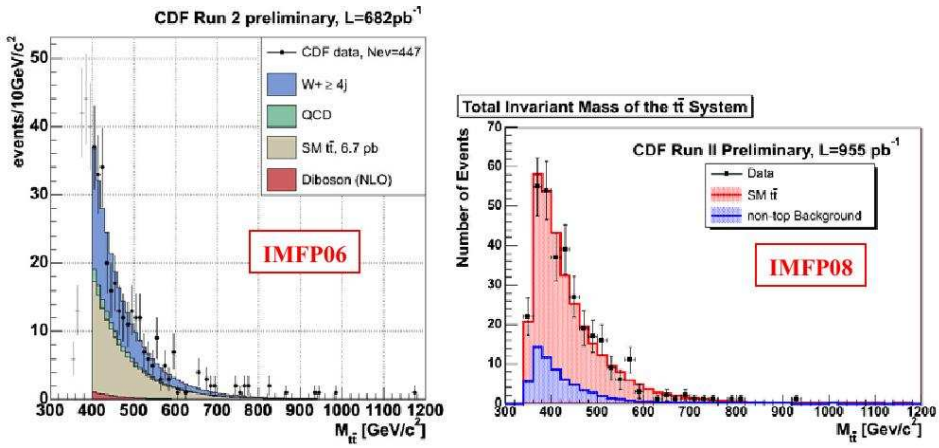

Fig. 79. Shows the CDF Run 2 $t\bar{t}$ invariant mass distribution with an integrated luminosity of 682 pb^{-1} (IMFP06, left) and 955 pb^{-1} (IMFP08, right).

DØ was the first to show significant evidence ($\approx 3.5\sigma$ effect) for single top production at the Tevatron (see Fig. 82). DØ was a bit lucky to see a signal with an integrated luminosity of 0.9 fb^{-1}. CDF did not see strong evidence for single top production until they had acquired 1.5 fb^{-1} as shown in Fig. 83. The production of single top in the t-channel has a kinematic peculiarity. As shown in Fig. 84, there is a distinct asymmetry in lepton charge Q times the pseudo-rapidity of the untagged jet. Fig. 85 shows a candidate t-channel single top event with $Q \times \eta = 2.9$ from CDF. It appears that we have found the single top needle in the haystack at the Tevatron. Fig. 86 shows the Tevatron single top cross-section measurements.

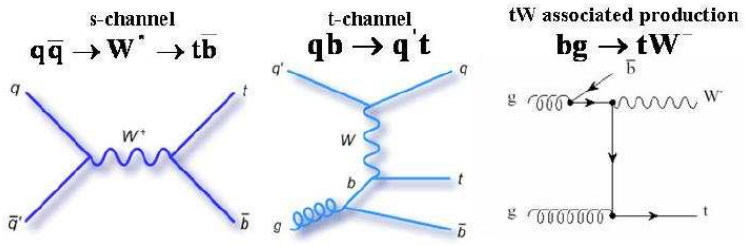

Fig. 80. Sources of single top production at the Tevatron. Single top quarks can be produced through s or t-channel W-boson exchange or produced in association with a top quark and a W-boson.

IMFP06

95% C.L. limits on single top cross-section

Channel	CDF (696 pb^{-1})	DØ (370 pb^{-1})
Combined	3.4 pb (2.9 pb)	
s-channel	3.2 pb (0.9 pb)	5.0 pb
t-channel	3.1 pb (2 pb)	4.4 pb

Single top discovery is possble in Run 2 at the Tevatron!

- R. Field (IMFP06)

Fig. 81. Tevatron limits at 95 % confidence level on single top production at 1.96 TeV for s-channel production, t-channel production, and combined as presented at IMFP06. The theory predictions are shown in parentheses.

We have discovered single top at the Tevatron and we are probing cross-section of less that 1 pb. I believe that new physics will soon be discovered at the Tevatron.

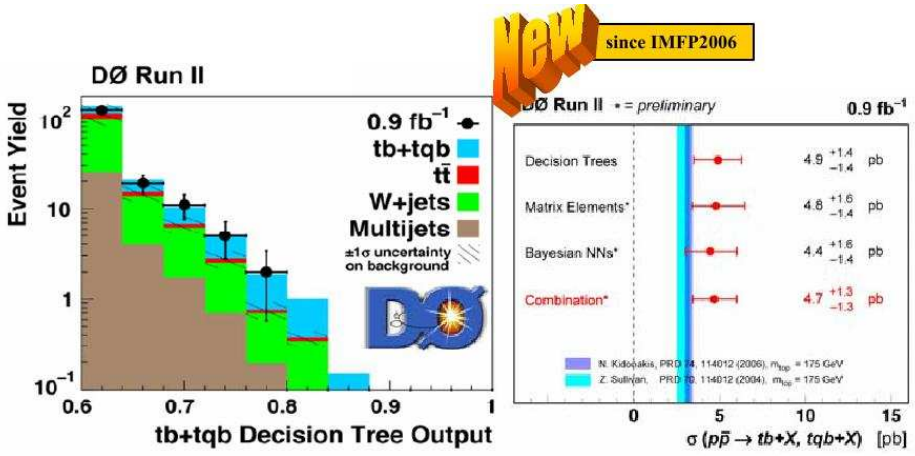

Fig. 82. (Left) evidence for single top production at 1.96 TeV from DØ with an integrated luminosity of 0.9 fb^{-1}. (Right) single top cross-sections at 1.96 TeV as measured by DØ . These results are new since IMFP06.

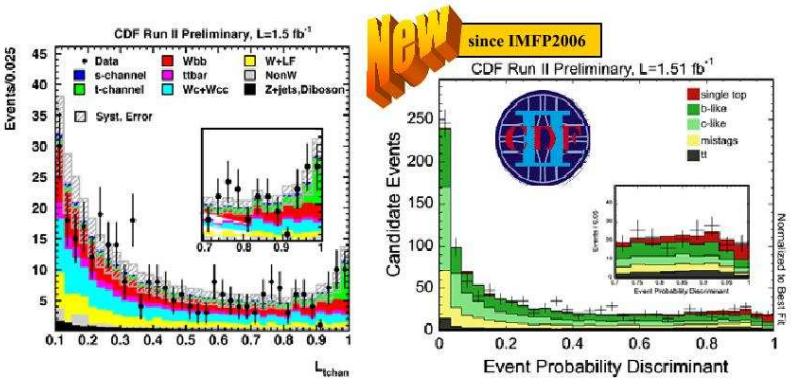

Fig. 83. Evidence for single top production at 1.96 TeV from CDF with an integrated luminosity of 1.51 fb^{-1}. These results are new since IMFP06.

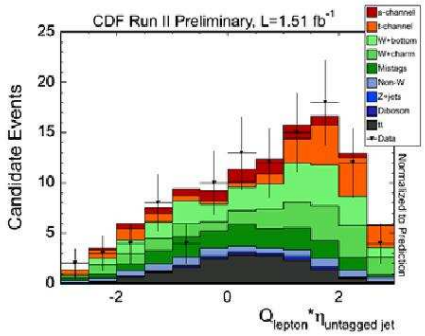

Fig. 84. Product of the lepton charge Q times the pseudorapidity of the untagged jet for t-channel single top candidate events at 1.96 TeV from CDF.

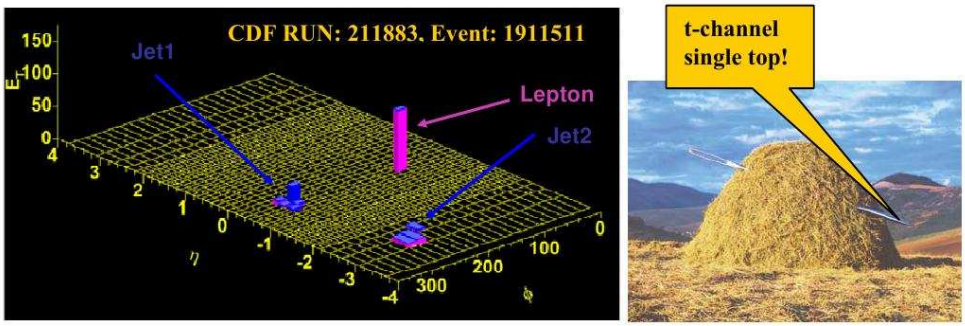

Fig. 85. (Left) CDF Run 2 t-channel single top candidate event (electron $\eta = -0.72$, $MET = 41.6\,\mathrm{GeV}$, $E_{\mathrm{T}}(b\text{-jet1}) = 46.7\,\mathrm{GeV}$, $\eta(b\text{-jet1}) = -0.6$, $E_{\mathrm{T}}(\mathrm{jet2}) = 16.6\,\mathrm{GeV}$, $\eta(\mathrm{jet2}) = -2.9$). (Right) finding the needle in the haystack.

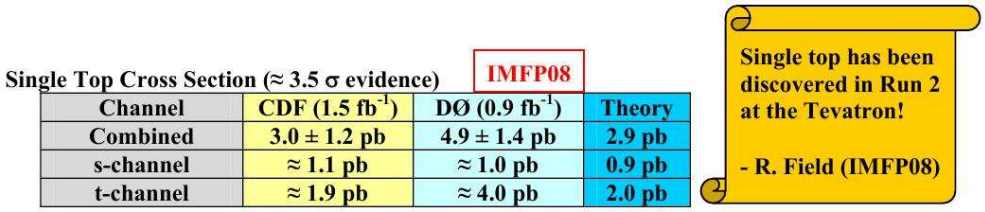

Fig. 86. Tevatron cross-sections measurements ($\approx 3.5\sigma$ evidence) for single top production at 1.96 TeV for s-channel production, t-channel production, and combined as presented at IMFP08.

I would like to congratulate F. del Aguila, A. Bueno, and N. García on organizing an excellent meeting. Also, I would like to thank my CDF colleagues who presented most of what I have shown here at the Winter conferences earlier this year.

REFERENCES

[1] Physics at the Tevatron, R. Field, FERMILAB-CONF-06-530-E, published in the proceedings of the XXXIV International Meeting on Fundamental Physics, El Escorial, Spain, April 2–7, 2006.

[2] R.D. Field, R.P. Feynman, *Phys. Rev.* **D15**, 2590 (1977).

[3] R.P. Feynman, R.D. Field, G.C. Fox, *Nucl. Phys.* **B128**, 1 (1977).

[4] R.D. Field, *Phys. Rev. Lett.* **40**, 997 (1978).

[5] R.P. Feynman, R.D. Field, G.C. Fox, *Phys. Rev.* **D18**, 3320 (1978).

[6] F. Paige, S. Protopopescu, BNL Report, BNL38034, 1986 (unpublished), version 7.32.

[7] G. Marchesini, B.R. Webber, *Nucl. Phys.* **B310**, 461 (1988); I.G. Knowles, *Nucl. Phys.* **B310**, 571 (1988); S. Catani, G. Marchesini, B.R. Webber, *Nucl. Phys.* **B349**, 635 (1991).

[8] T. Sjostrand, *Phys. Lett.* **157B**, 321 (1985); M. Bengtsson, T. Sjostrand, M. van Zijl, *Z. Phys.* **C32**, 67 (1986); T. Sjostrand, M. van Zijl, *Phys. Rev.* **D36**, 2019 (1987).

[9] B. Andersson, G. Gustafson, G. Ingelman, T. Sjostrand, *Phys. Rep.* **97**, 31 (1983).

[10] T. Affolder *et al.* [CDF Collaboration], *Phys. Rev.* **D65**, 092002 (2002).

[11] The Underlying Event in Large Transverse Momentum Charged Jet and Z-boson Production at 1.8 TeV, talk presented by Rick Field at DPF2000, Columbus, OH, August 11, 2000.

[12] A Comparison of the Underlying Event in Jet and Min-Bias Events, talk presented by Joey Huston at DPF2000, Columbus, OH, August 11, 2000. The Underlying Event in Jet and Minimum Bias Events at the Tevatron, talk presented by Valeria Tano at ISMD2001, Datong, China, September 1–7, 2001.

[13] J. Pumplin, *Phys. Rev.* **D57**, 5787 (1998).

[14] D. Acosta *et al.* [CDF Collaboration], *Phys. Rev.* **D70**, 072002 (2004).

[15] F. Abe *et al.* [CDF Collaboration], *Phys. Rev. Lett.* **67**, 2937 (1991).

[16] The value of PARP(62), PARP(64), and PARP(91) was determined by CDF Electroweak Group. The "W" in Tune AW, BW, DW, DWT, QW stands for "Willis". I combined the "Willis" tune with Tune A, *etc.*

[17] V.M. Abazov *et al.* [DØ Collaboration], *Phys. Rev. Lett.* **94**, 221801 (2005).

[18] J.M. Butterworth, J.R. Forshaw, M.H. Seymour, *Z. Phys.* **C7**, 637 (1996).

[19] M. Cacciari, *et al.*, *J.High Energy Phys.* **068**, 0404 (2004) [hep-ph/0303085].

[20] B.W. Harris, E. Laenen, L. Phaf, Z. Sullivan, S. Weinzierl, *Phys. Rev.* **D66**, 054024 (2002); Z. Sullivan, *Phys. Rev.* **D70**, 114012 (2004); T. Tait, *Phys. Rev.* **D61**, 034001 (2000); A. Belyaev, E. Boos, *Phys. Rev.* **D63**, 034012 (2001).